Adv. Polar Upper Atmos. Res., 13, 1-36, 1999

QUANTITATIVE RING CURRENT MODEL: OVERVIEW AND COMPARISON WITH OBSERVATIONS

Yusuke EBIHARA[1,2] and Masaki EJIRI[3]

[1] *Department of Polar Science, the Graduate University for Advanced Studies, Kaga 1-chome, Itabashi-ku, Tokyo 173-8515*

[2] *Now at Swedish Institute of Space Physics, Box 812, S-981 28 Kiruna, Sweden*

[3] *National Institute of Polar Research, Kaga 1-chome, Itabashi-ku, Tokyo 173-8515*

Abstract: This paper describes a new quantitative ring current model that solves temporal evolution of the ion distribution in the magnetosphere by tracing the ion drift motion. The plasma sheet density as a boundary condition of our model depends on the solar wind density. The tracing is performed under a dipole magnetic field and a time-dependent convection electric field depending on the solar wind parameters. The ions are lost by two processes; the charge exchange with neutral hydrogen and the convection outflow due to encounter with the dayside magnetopause. Magnetic disturbance is directly derived from the calculated current density with the three-dimensional Biot-Savart integral; this is a new simulation method. Using this model, we have examined the physical mechanism of the storm-time ring current responding to the interplanetary parameters. We simulated three successive storms which occurred in April 1997 as a case study. The following subjects concerned with dynamics of the ring current were examined; (1) the causes of the ring current development, (2) the electric current distribution, (3) the effects of the charge exchange loss, (4) the energy composition of the plasma pressure, (5) the response time lag of the plasma sheet density variation to the solar wind density and (6) the diamagnetic effect.

1. Introduction

The terrestrial ring current mainly consists of trapped energetic ions with energies 10–200 keV (FRANK, 1967; SMITH and HOFFMAN, 1973; WILLIAMS, 1981). The global intensity of the ring current can be monitored by the ground-based magnetic observation at mid- and low-latitudes. The *Dst* index calculated from the observed geomagnetic field gives a zeroth-order estimate of the ring current intensity. Occasionally extra particles are transported (or injected) from the magnetotail into the ring current region by a large-scale convection field, and they are adiabatically energized. Consequently, the enhanced current depresses the *Dst* value. The total ring current energy has been estimated from the decrease of the *Dst* value using the Dessler-Parker-Sckopke relation (DESSLER and PARKER, 1959; SCKOPKE, 1966). Considering total kinetic energy in the ring current region, several empirical models have been proposed to explain the depression of storm-time *Dst* (e.g., BURTON *et al.*, 1975; GONZALEZ *et al.*, 1989). The empirical models suggest that the *Dst* decrease can be expressed by a function of the southward component of interplanetary magnetic field (IMF) and the solar wind bulk

velocity.

In order to understand a physical process for the ring current development and its decay, it is useful to trace trajectories of the ions that contribute to the ring current. Many models of the ring current development have been proposed (*e.g.*, LEE *et al.*, 1983; WODNICKA, 1989; TAKAHASHI *et al.*, 1990; FOK *et al.*, 1993, 1995, 1996; CHEN *et al.*, 1994; JORDANOVA *et al.*, 1994, 1998; BOURDARIE *et al.*, 1997; KOZYRA *et al.*, 1998a, b). Recently, JORDANOVA *et al.* (1998) and KOZYRA *et al.* (1998a, b) have pointed out that the superdense plasma sheet plays an important role in the ring current buildup during magnetic storms.

After examining the relationship between the solar wind density and the near-earth plasma sheet density, BOROVSKY *et al.* (1997, 1998) and TERASAWA *et al.* (1997) have concluded that they are highly correlated. This means that the near-earth plasma sheet density is well responsive to the change in the solar wind density. If the plasma sheet density is positively correlated with the solar wind density, the enhanced solar wind density could resultantly cause the ring current buildup. As evidence of that, THOMSEN *et al.* (1998) statistically examined their relationship and they have concluded that an increase in the solar wind density is positively correlated with the ring current buildup. Using our particle tracing code, the ring current development as a function of the solar wind parameters is discussed in this paper. Our ring current model solves each particle's drift motion under a dipolar magnetic field and a time-dependent convection electric field. After tracing the drift motion, we calculate the three-dimensional distribution of the differential flux, the plasma pressure and the current density in the ring current region. The magnetic disturbance at the center of the earth can be derived with the Biot-Savart law from the whole three-dimensional distribution of the calculated current density; this is a new simulation method. Therefore our model can calculate the spatial and temporal changes of the particle distribution, the pressure, the current density and the magnetic disturbance as a function of physical parameters in the interplanetary space.

Several processes have been proposed to explain the global ring current enhancement empirically and theoretically; (1) the inward transport of plasma sheet particles by the enhanced convection electric field (*e.g.*, WILLIAMS, 1981; WODNICKA, 1989; TAKAHASHI *et al.*, 1990; LUI, 1993; BOURDARIE *et al.*, 1997; WOLF *et al.*, 1997; JORDANOVA *et al.*, 1998; EBIHARA and EJIRI, 1998), (2) the particle injection associated with a substorm (*e.g.*, KAMIDE and FUKUSHIMA, 1971; LUI *et al.*, 1987; FOK *et al.*, 1996; EBIHARA *et al.*, 1998b), (3) the diffusive transport of energetic particles due to the magnetic and/or electric fluctuation (*e.g.*, LYONS and SCHULZ, 1989; RILEY and WOLF, 1992; LUI, 1993; CHEN *et al.*, 1993, 1994, 1998; BOURDARIE *et al.*, 1997), (4) the inward displacement of pre-existing trapped particles due to an enhanced electric field (*e.g.*, LYONS and WILLIAMS, 1980), (5) the direct entry of ions from the polar region into the ring current (*e.g.*, SHELLEY *et al.*, 1972, 1976; PARKS *et al.*, 1977; CLADIS and FRANCIS, 1985; DELCOURT *et al.*, 1990; PEROOMIAN and ASHOUR-ABDALLA, 1996). In this paper, we examine the process (1); the development of the ring current is caused by the inward transport of plasma sheet particles. The contribution of electrons to the ring current is not discussed in this paper because the energy density of electrons is less than that of protons by a factor of 5-6 in the ring current region (*e.g.*, FRANK, 1967). This lower

energy density of electrons may be caused by the lower temperature in the plasma sheet. Satellite observations have reported that the plasma sheet temperature of electrons is less than that of ions by a factor of 5-7 (*e.g.*, BAUMJOHANN *et al.*, 1989).

Unless otherwise mentioned MKS units are used throughout this paper.

2. Model Description

2.1. *Source distribution function*

We first examine the relationship between the solar wind density and the plasma sheet density at the geocentric distance of 9–11 Re, which is the region for the ring

Table 1. Criteria for the selection of GEOTAIL and WIND data sets.

GEOTAIL LEP	available
MLT of GEOTAIL	21 h–3 h
Radial distance of GEOTAIL	9–11 Re
|GSM-Z| of GEOTAIL	<2 Re
Radial distance of WIND	>15 Re
Ion beta ($=2\mu_0 nkT/B^2$)	>0.8

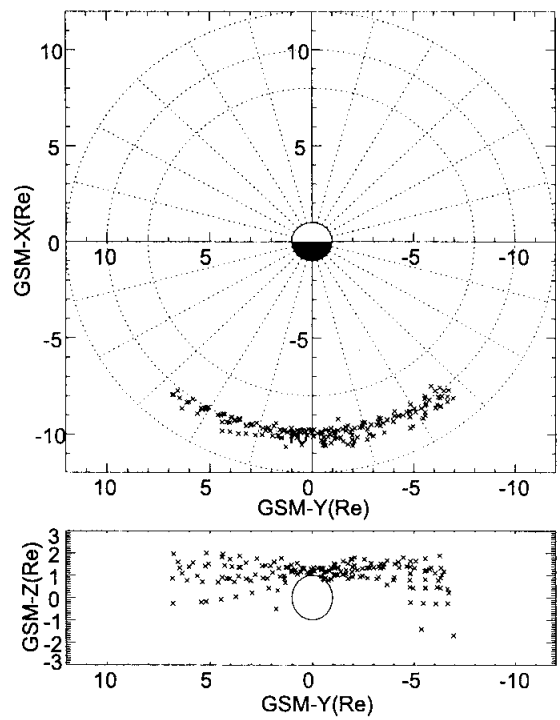

Fig. 1. Position of GEOTAIL satisfying the criteria in 1995–1997. Top and bottom panels show the position in the GSM-X-Y plane and the GSM-Y-Z plane, respectively.

current boundary. The number density and the temperature of ions in the plasma sheet are provided by GEOTAIL LEP (MUKAI *et al.*, 1994) with the energy-per-charge analyzer (EA-ion) which gives three-dimensional velocity distributions of ions over the energy range of 32 eV/q–39 keV/q. The criteria to select the available data sets are listed in Table 1. To exclude the data observed in the lobe, the high ion beta value is added to the criteria; the ion beta is defined as $2\mu_0 N_{ps} kT/B^2$, where μ_0 is the permeability in vacuum, N_{ps} the plasma sheet density, k the Boltzmann constant, T the temperature and B the intensity of the magnetic field. The local magnetic field data are provided by GEOTAIL MGF (KOKUBUN *et al.*, 1994). The data during the period of umbras and penumbras of GEOTAIL are excluded. We found 170 thirty-minute intervals that satisfied the criteria in 1995–1997. Position of the thirty-minute intervals of GEOTAIL satisfying the criteria is shown in Fig. 1. The solar wind and IMF data sets are provided by SWE (OGILVIE *et al.*, 1995) and MFI (LEPPING *et al.*, 1995) instruments aboard the WIND satellite, respectively. A time lag from WIND to the earth is adjusted by assuming that the solar wind velocity is fixed to be 400 km/s. However, the delay of the penetration of the solar wind medium into the plasma sheet is not adjusted here.

The result of the statistical analysis is shown in Fig. 2. The plasma sheet density N_{ps} at the geocentric distance of 9–11 Re is well correlated with the solar wind density N_{sw}; the result is consistent with the previous studies that the plasma sheet densities at the geosynchronous altitude and the geocentric distance of 17.5–22.5 Re (BOROVSKY *et al.*, 1997) and the geocentric distance of 15–50 Re (TERASAWA *et al.*, 1997) are also well correlated with the solar wind density. The data indicated in Fig. 2 can be fitted by $N_{ps} = 0.025 N_{sw} + 0.395$ (cm^{-3}) with a linear correlation coefficient of 0.75 and the fitted equation is used to estimate the plasma sheet density at the geocentric distance of 10 Re for the boundary condition of this ring current model.

The distribution function at the model boundary located at 10 Re is assumed to be isotropic and Maxwellian. The temperature at the boundary is fixed to be 5 keV and the number density N_{ps} is given by the fitted equation described above.

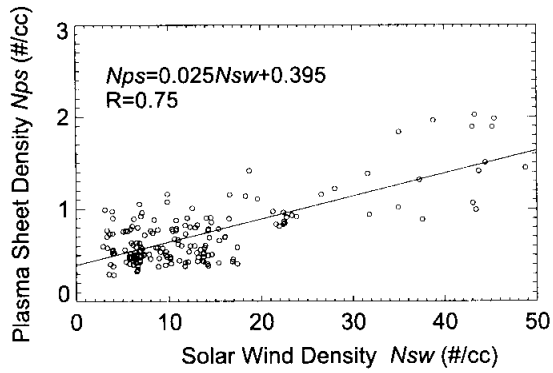

Fig. 2. The plasma sheet density at the geocentric distance of 9–11 Re (N_{ps}) as a function of the solar wind density (N_{sw}).

2.2. Convection electric field

Recently, BOYLE *et al.* (1997) reexamined solar wind coupling functions in the literature using more than 58000 polar passes of DMSP with strict criteria to provide updated estimates of the polar cap potential. They found the function expressed as

$$\Phi_{PC} = -4.1 + 0.5\sin(\phi + 0.056 + 0.015 B_y(\mathrm{nT})) \times (1.1\times 10^{-4} V_{sw}(\mathrm{km/s})^2 + 11.1 B_{IMF}(\mathrm{nT})\sin^3(\theta_{IMF}/2))\ (\mathrm{kV}), \quad (1)$$

where Φ_{PC} is the polar cap potential, ϕ the magnetic local time (MLT), B_y the GSM-Y component of IMF, V_{sw} the bulk velocity of the solar wind, B_{IMF} the magnetic intensity of IMF and θ_{IMF} the polar angle of IMF. After removing the skewed angle of the potential, we applied the polar cap potential drop expressed in eq. (1) to the Volland-Stern type convection field model (VOLLAND, 1973; STERN, 1975) with a shielding factor of 2 in the equatorial plane as

$$\Phi \approx [1.1\times 10^{-4} V_{sw}(\mathrm{km/s})^2 + 11.1 B_{IMF}(\mathrm{nT})\sin^3(\theta_{IMF}/2)] \frac{\sin\phi}{2}\left(\frac{R}{R_B}\right)^2(\mathrm{kV}), \quad (2)$$

where Φ, R and R_B are the electric potential, the geocentric distance at a given point and the geocentric distance of the magnetopause at 0600 MLT or 1800 MLT, respectively. In a dipole magnetic field, the geocentric distance of the magnetosphere boundary R_B in the equatorial plane is given by

$$R_B = \frac{1}{\cos^2\lambda_{PC}}\ (\mathrm{Re}), \quad (3)$$

where λ_{PC} is a latitude of the polar cap boundary. λ_{PC} is taken to be 72° and then R_B is 10.47 Re; the magnetosphere boundary R_B is assumed to be steady in this simulation. According to the statistics, the assumed polar cap boundary latitude of 72° in the dawn and dusk meridians is consistent with the poleward boundary of the closed region for active periods (MAKITA *et al.*, 1983).

2.3. Loss processes

The ions are lost by two processes; the charge exchange with neutral hydrogen and the convection outflow to the dayside magnetopause azimuthally located at $L=10$. The Coulomb collision loss with thermal plasmas is neglected (EBIHARA *et al.*, 1998a).

The charge exchange is one of the major loss processes of the ring current ions (*e.g.*, FRANK, 1967; SWISHER and FRANK, 1968; PRÜLSS, 1973; SMITH *et al.*, 1976, 1981; TINSLEY, 1976; LYONS and EVANS, 1976; SMITH and BEWTRA, 1978; KISTLER *et al.*, 1989; FOK *et al.*, 1993; NOËL, 1997). The change of the phase space density f due to the charge exchange loss is expressed as

$$\frac{\partial f}{\partial t} = -\frac{f}{\tau_{ce}}, \quad (4)$$

where τ_{ce} is the charge exchange lifetime. We calculate $\partial f/\partial t$ along particles' bounce-averaged trajectories. The bounce-averaged charge exchange lifetime can be expressed as

$$\tau_{ce} \simeq \frac{\cos^j \lambda_m}{n'_H \sigma_H v}, \tag{5}$$

where λ_m is the mirror latitude, n'_H the equatorial density of the neutral hydrogen, σ_H the charge exchange cross section and v the speed of an ion. Following SMITH and BEWTRA (1978), the value j is given to be 3.5. A spherically symmetric model derived by CHAMBERLAIN (1963) with its parameters given by RAIRDEN *et al.* (1986) is applied to obtain the equatorial number density of the neutral hydrogen n'_H. We use the charge exchange cross section σ_H from JANEV and SMITH (1993).

2.4. *Overview of the scheme*

The simulation scheme is schematically summarized in Fig. 3. All ions are injected through the 'injection boundary' azimuthally located at $L=10$ with 2100–0300 MLT. After tracing the ions under a dipole magnetic field, the corotation electric field

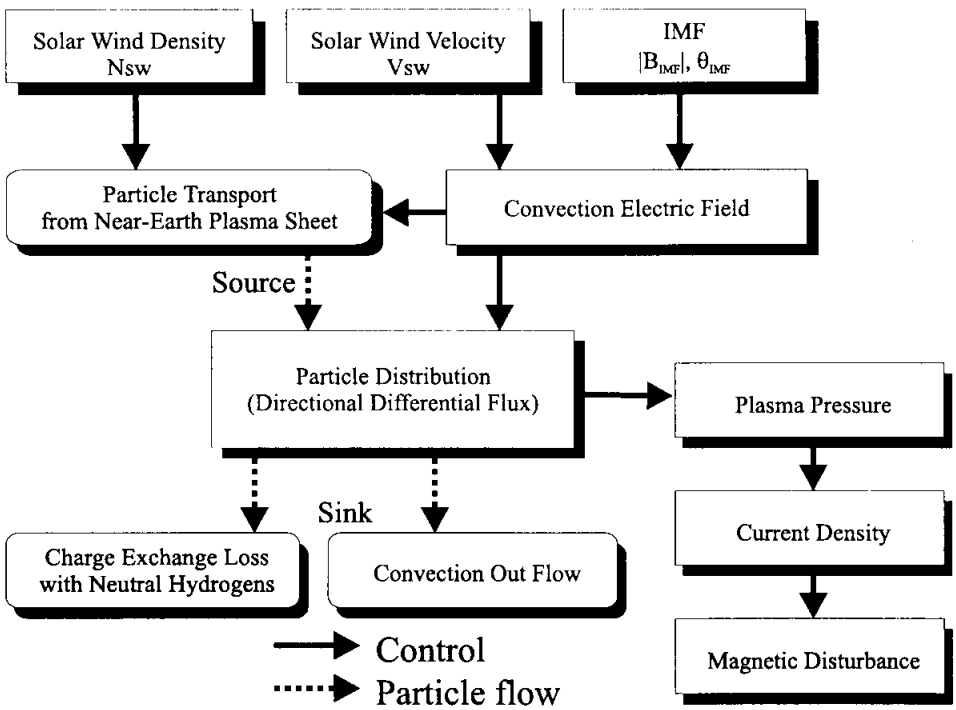

Fig. 3. A block diagram of this simulation that depends on the solar wind and IMF as input parameters. Rectangles and round rectangles indicate physical quantities and physical process, respectively. The primary output of this simulation is the directional differential flux in the equatorial plane.

and the Volland-Stern type convection field with its intensity depending on the solar wind velocity and IMF, the directional differential flux, the plasma pressure and the current density are calculated. The magnetic disturbance induced by the current density can be directly obtained with the Biot-Savart integral from the whole three-dimensional distribution of the calculated ring current. The bounce-averaged drift velocity and the details of the derivation of the macroscopic quantities (the differential flux, the plasma pressure and the current density) are given in Appendix A.

3. Results

We simulated three successive magnetic storms, which occurred in April 1997, and compared the calculated results to the observed values of pressure corrected *Dst*. The pressure corrected *Dst* (hereinafter referred to as *Dst**) is given by

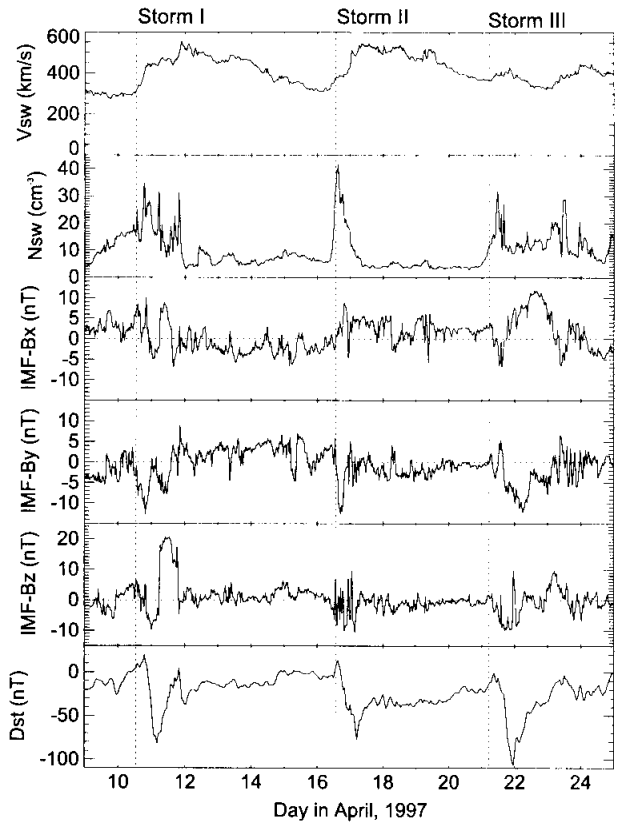

Fig. 4. The solar wind, IMF and Dst during a period the storms on April 9–25, 1997. From the top to the bottom panels, the solar wind bulk velocity V_{sw}, the number density of the solar wind protons N_{sw}, the GSM-X, -Y and -Z components of the IMF and observed Dst are shown. Vertical lines indicate the start times of the storms.

$$Dst^* = (Dst - c_1 P_{sw}^{1/2} + c_2)/\xi , \tag{6}$$

where P_{sw} is the dynamic pressure of the solar wind, ξ a coefficient for the earth's induction, and c_1 and c_2 are empirical coefficients, respectively. Typically, the coefficients, c_1 and c_2, are 0.2 nT/(eV cm^{-3})$^{1/2}$ and 20 nT, respectively (*e.g.*, GONZALEZ *et al.*, 1994). After DESSLER and PARKER (1959), the coefficient for the induction ξ is taken to be 1.5. The solar wind bulk velocity (V_{sw}), the solar wind proton number density (N_{sw}), the GSM-X, -Y and -Z components of the interplanetary magnetic field (IMF-Bx, -By and -Bz), and the observed *Dst* index during the storms are plotted in Fig. 4. These interplanetary parameters are obtained from SWE and MFI instruments aboard the WIND satellite. There were three major storms in April 1997; the storms began at 1300 UT on April 10, 1997 (hereinafter denoted as Storm I), at 1320 UT on April 16 (Storm II) and at 0500 UT on April 21 (Storm III), which are indicated by vertical lines in Fig. 4. The minima of *Dst* are −82 nT, −77 nT and −107 nT, respectively; the storms were categorized as moderate to intense ones. Especially, Storm III was caused by a passage of a huge magnetic cloud with an estimated diameter of 0.4 AU (R. LEPPING, personal communication, 1998).

3.1. *Dst*

In Fig. 5, the calculated *Dst** is compared with the observed one during the period

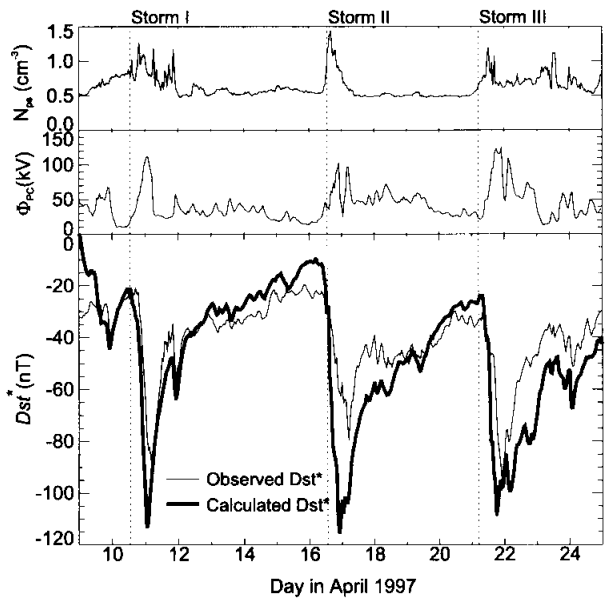

Fig. 5. Comparison between calculated and observed Dst. From the top panel, the plasma sheet number density deduced from the solar wind density, the polar cap potential drop derived by BOYLE et al. (1997) and calculated Dst* (thick line) with observed Dst* (dotted line) during the period of April 9–25, 1997 are shown.*

of April 9–25, 1997. We adjust the offset of the observed *Dst** at the beginning of the Storm I (April 10, 1997, 1300 UT) to the calculated *Dst** at this time. Because the magnetosphere is initially empty in our calculation, the curve of calculated *Dst** starts with *Dst** of 0 at 0000 UT on April 9, 1997. As demonstrated in Fig. 5, the calculated *Dst** roughly tracks the observed *Dst**. The calculated *Dst** tends to overshoot the observed one. The recovery of the calculated *Dst** takes place earlier than the observed *Dst** by 5–7 hours. The difference between calculated and observed *Dst** will be discussed in Section 4.

3.2. Energy input rate

Number of ions passing through the 'injection boundary' depends on the polar cap potential Φ_{PC} and the plasma sheet number density N_{ps} in this simulation. To examine both contributions to the ring current buildup as indicated by *Dst**, two cases are examined; one is a case under the steady convection with Φ_{PC} of 20 kV, and the other is a case under the steady plasma sheet density with N_{ps} of 0.4 cm^{-3}.

Figure 6 shows the results. The calculated *Dst** keeping the plasma sheet density constant (the thick and solid line) tends to undershoot the observed one around the most disturbed periods. This may suggest that the enhancement of the plasma sheet density is needed especially for the Storm I and the Storm III. The calculated *Dst** keeping the polar cap potential constant (the thick and dashed line) little agrees with the observed

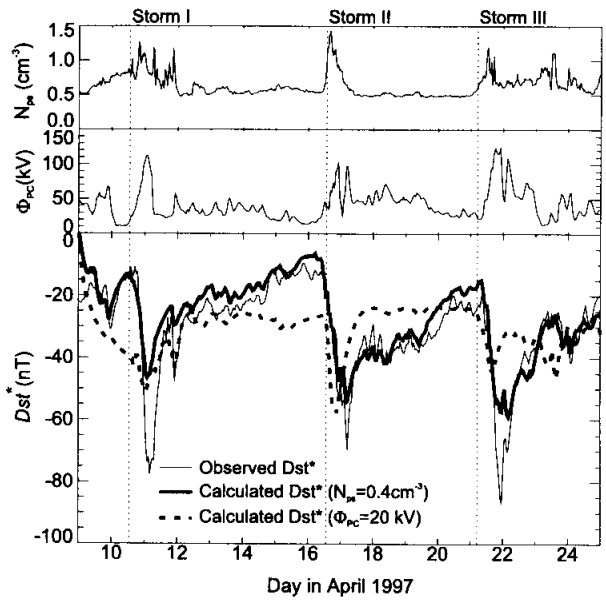

Fig. 6. Plasma sheet density (top), polar cap potential drop (middle) and Dst (bottom). Three curves in the bottom panel indicate observed Dst* (thin line), calculated Dst* with steady convection field of 20 kV (thick and dashed line) and calculated Dst* with steady plasma sheet density of 0.4 cm^{-3} (thick and solid line), respectively.*

one.

The result can be explained by an analytical expression. The energy input rate into the ring current is analytically given by

$$\gamma = 0.572 N_{ps}(\mathrm{cm}^{-3}) E_0(\mathrm{keV}) \Phi_{PC}(\mathrm{kV}) \text{ (gigawatt)}, \tag{7}$$

where E_0 is the plasma sheet temperature. The derivation of eq. (7) is described in Appendix B. Equation (7) indicates that the energy input rate is proportional to the number density in the plasma sheet (N_{ps}) times the temperature in the plasma sheet (E_0) times the polar cap potential drop (Φ_{PC}).

Because the plasma sheet temperature is insensitive to *Dst** as examined below, the energy input rate γ is approximately a function of the plasma sheet density N_{ps} and the polar cap potential Φ_{PC}. If the plasma sheet temperature E_0 is fixed to be 5 keV, the energy input rate becomes simply as

$$\gamma = 2.86 N_{ps}(\mathrm{cm}^{-3}) \Phi_{PC}(\mathrm{kV}) \text{ (gigawatt)}. \tag{8}$$

For a typical case in the main phase of a storm, N_{ps} is 1.5 cm^{-3} and Φ_{PC} 120 kV. Then the energy input rate becomes 520 gigawatts.

3.3. *Dependence on the plasma sheet temperature*

As described in the previous subsection, the analytic expression of the energy input rate into the ring current eq. (7) indicates that the energy input rate is a function of N_{ps}, E_0 and Φ_{PC}. As the plasma sheet temperature increases, the relative number of high energy ions increases but the relative number of low energy ions decreases. Because high energy ions tend to drift azimuthally, they hardly move towards the earth.

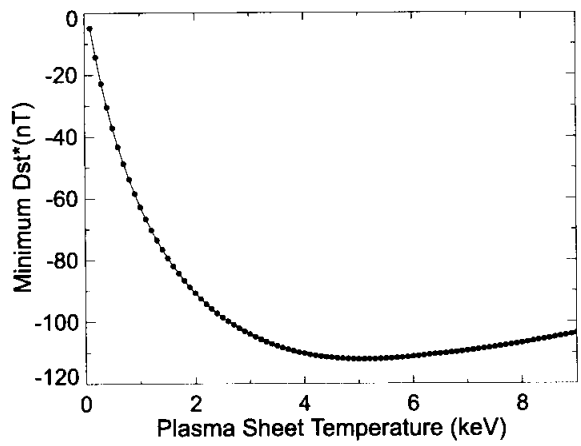

Fig. 7. Temperature dependence of the ring current buildup. The curve in the diagram indicates the minimum Dst as a function of the plasma sheet temperature for Storm I occurred on April 10–11, 1997.*

Therefore these ions flow away from the magnetosphere and they contribute slightly to the ring current buildup. Consequently, the ring current intensity as indicated by *Dst** could not simply be proportional to the plasma sheet temperature.

Figure 7 shows a variation of the minimum *Dst** of Storm I as a function of the plasma sheet temperature E_0 keeping the plasma sheet density constant. As demonstrated in Fig. 7, the ring current buildup as indicated by *Dst** is insensitive to the temperature in the near-earth plasma sheet for the temperature above 3 keV. However, for the temperature below 3 keV, minimum *Dst** is sensitive to the plasma sheet temperature.

According to the statistics of the direct satellite observations, the average temperature in the near-earth plasma sheet is ~5 keV (*e.g.*, BAUMJOHANN *et al.*, 1989; PATERSON *et al.*, 1998), except during a substorm expansion phase. During the substorm expansion, BAUMJOHANN (1996) and BIRN *et al.* (1997) reported that the temperature in the near-earth plasma sheet increases. According to BOROVSKY *et al.* (1998), the plasma sheet temperature at 17.5–22.5 Re is higher than 3 keV for the solar wind velocity > 350 km/s. Therefore, we concluded that the ring current buildup during a storm is insensitive to the change of the plasma sheet temperature.

3.4. Electric current distribution

Figure 8 illustrates the temporal evolution of the plasma pressure perpendicular to the magnetic field ($P_\perp$) and the current density perpendicular to the magnetic field ($J_\perp$) in the equatorial plane for Storm I. There are two characteristics to be noted:

1) As the storm develops at 0100 UT on April 11 (labeled as *B*), the plasma pressure drastically increases in the dusk region; the peak is located at 5.1 Re with the perpendicular plasma pressure of 34 nPa, Both westward and eastward currents are also enhanced simultaneously. The peak of the eastward current is located at 4.4 Re and the westward current at 6.9 Re. The spatial structure of the current density is essentially asymmetric.
2) In the recovery phase at 0700 UT on April 11 (labeled as *C*), the previously enhanced plasma pressure and the current density decrease. The peak of the plasma pressure is still located at 5.3 Re, but the pressure decreases to 18 nPa. The spatial structure of the current density is getting more symmetric.

The asymmetric structure (during the main phase) and the symmetric structure (during the recovery phase) were observed by the NOAA-12 satellite. Figure 9 shows daily averaged count rates of protons with an energy range of 30–80 keV observed by NOAA-12 (the daily averaged data, courtesy of Y. MIYOSHI) during a period of April 9 –13, 1997. Here we regard that the daily averaged count rate of the protons with a energy range of 30–80 keV gives the relative intensity of the core ring current. NOAA-12 is the polar orbiting satellite with an altitude of 815 km and an inclination of 98°. The Medium Energy Proton and Electron Detector (MEPED) has solid state detector telescopes within the energy ranges of 30–80, 80–250, 250–800 and 800–2500 keV. One telescope views radially outward along the earth-satellite vector. Another telescope views in a direction perpendicular to the first one. Therefore the latter telescope observes trapped particles at high latitudes. Each line in Fig. 9 indicates the count rates of the protons measured by the telescope viewing the perpendicular direction to the

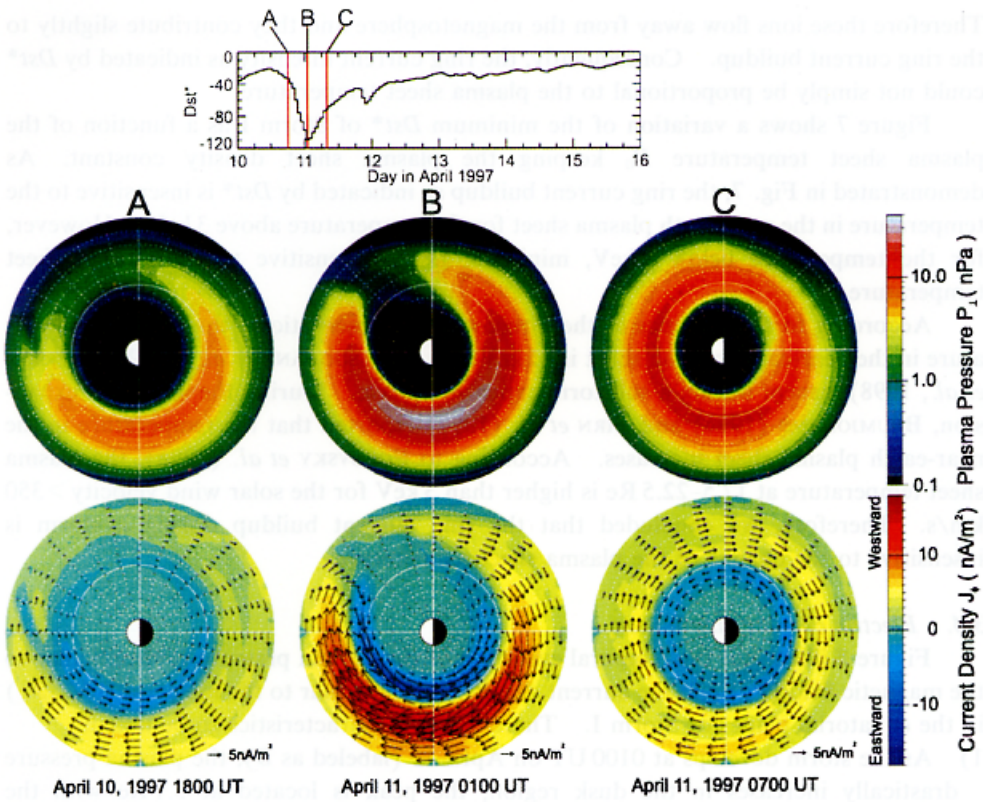

Fig. 8. Snapshots of the equatorial pressure and the current density in Storm I. Top panel shows calculated Dst. Middle and bottom panels show the pressure perpendicular to the magnetic field and the current density perpendicular to the magnetic field in the equatorial plane, respectively, at 1800 UT on April 10, 1997 (left panels; denoted as A), 0100 UT on April 11, (middle panels; B) and 0700 UT on April 11, 1997 (right panels; C). In the bottom panels (current density), the pseudo-color code indicates the strength of the azimuthal component of the current density; red as westward and blue as eastward currents. Arrows indicate the direction of the current.*

earth-satellite vector. A noticeable enhancement of counts in the dusk region could be seen during the main and the early recovery phases (April 10–11, 1997). The counts in the dusk region exceeded ~2000, which were greater than the counts in the dawn region by a factor of 6–7. The dawn-dusk asymmetry suggests that most of the protons transported from the night side plasma sheet escape from the ring current region, *i.e.*, the protons, which enhance the counts in the dusk region, hardly drift into the dawn region through the dayside region. In the recovery phase, particular protons began drifting around the earth under a weakened convection field, and then the symmetric structure of the ring current located at $L=4$–5 remained in the dawn and dusk regions. It is also noticeable in Fig. 9 that the L-values of the most enhanced counts in the dawn region were somewhat larger than those of the counts in the dusk region. A theoretical

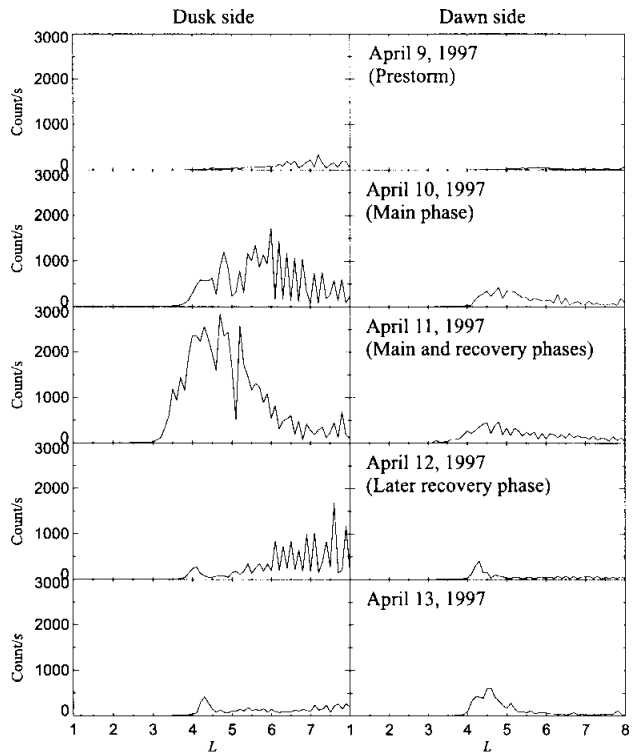

Fig. 9. Daily averaged count rates of protons with an energy range of 30–80 keV. The data were obtained by the polar orbitting satellite, NOAA-12. From top to bottom, each panel indicates the count rates as a function of L during a period from April 9, 1997 to April 13. Left panels show the proton count rates in the dusk region (2000 MLT) and right panels show them in the dawn region (0800 MLT).

calculation suggests that the closed drift trajectories of the protons are not exactly symmetric (see Fig. A1); they are swelled in the dawn region. The difference of the peaks observed by NOAA-12 in the dawn and dusk region can be explained by considering the swelled drift trajectories of the protons. We cannot quantitatively discuss the details of the observed data because they are the data observed at high latitudes. NOAA-12 cannot measure the bulk of the ring current protons which are bouncing near the equatorial region.

The calculated cross sections of the electric current and the plasma pressure in the equatorial plane at 1800 MLT are presented in Fig. 10. Four curves in the top panel in Fig. 10 indicate the total azimuthal current density J_ϕ, the magnetization current density J_M, the curvature drift current density J_R and the grad-B drift current density J_B, respectively. Since the anisotropy of the plasma pressure is relatively small ($P_\parallel/P_\perp \sim 1.2$), the azimuthal current density J_ϕ is mainly produced by the $\nabla P_\perp$ term in eq. (A 20) because the second term on the right hand side of eq. (A20) can be negligible.

Next, the contribution of the eastward and the westward currents to *Dst** are

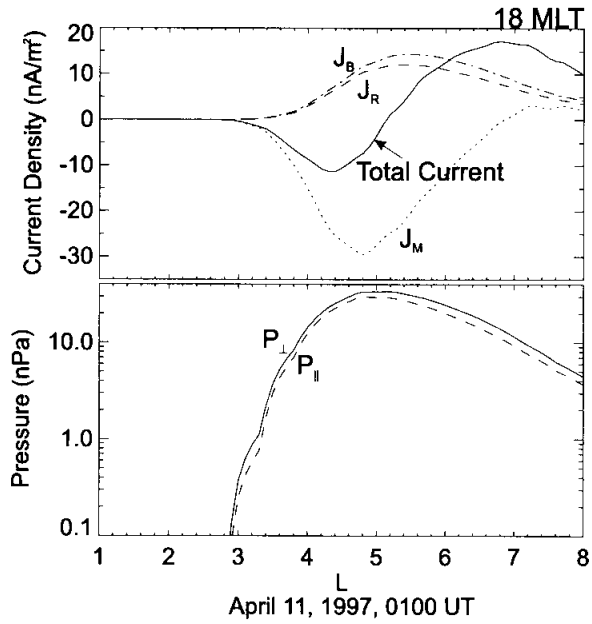

Fig. 10. Cross sections of the equatorial current density (top panel) and plasma pressure (bottom panel) as a function of L in the meridian at 1800 MLT at 2200 UT on April 10, 1997. In the top panel, solid, dotted, dashed and dashed-dotted lines indicate the total azimuthal current J_ϕ, the magnetization current J_M, the curvature drift current J_R and the grad-B drift current J_B, respectively. The positive value denotes the westward current. In the bottom panel, a solid line indicates the perpendicular plasma pressure $P_\perp$ and a dashed line the parallel plasma pressure $P_\parallel$.

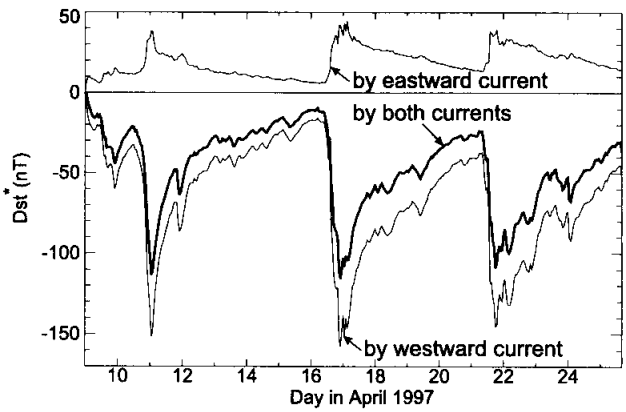

Fig. 11. Calculated Dst induced by the westward current (thin line; denoted as 'westward'), by the eastward current (thin line; denoted as 'eastward') and by the both currents (thick line; denoted as 'both') during the period of April 9–25, 1997.*

examined. The total current density J_ϕ has peaks at $L=4.4$ for the eastward current ($12\,nA/m^2$) and at $L=6.9$ for the westward current ($17\,nA/m^2$). These current densities resemble each other. However, the total current flows westward because of its larger volumes than that of the eastward current, and hence, *Dst** decreases. Three lines in Fig. 11 indicate *Dst** induced by the westward current, the eastward current and both currents, respectively. The intensity of *Dst** induced by the westward current is larger than *Dst** induced by the eastward current by a factor of 3–4.

3.5. *Effects of charge exchange loss*

The loss effect of energetic ions in the ring current region due to the charge exchange is examined here. The charge exchange loss effect on the *Dst** during the storms is clearly shown in Fig. 12. The dotted line indicates the calculated *Dst** without the charge exchange loss, *i.e.*, the convection outflow is the only loss process. The initial rapid recovery of the *Dst** at the beginning of the recovery phase can be seen in both with the charge exchange and without the charge exchange. This means that the initial rapid recovery in the early recovery phase is mainly due to (1) the temporal change of the spatial structure and (2) the sudden decrease of the plasma sheet density. We will discuss the cause of the initial rapid recovery in future. After the initial rapid recovery, the *Dst** decays slowly due to the charge exchange in the late recovery phase. The recovery rate of the calculated *Dst** with the charge exchange is in good agreement with that of the observed one. On the other hand, the *Dst** without the charge exchange hardly recovers in the late recovery phases; the next storm occurs before the

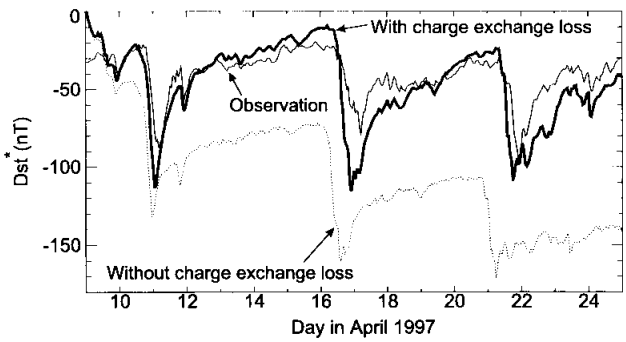

Fig. 12. Charge exchange loss effect on Dst. Observed Dst* (thin line), calculated Dst* with charge exchange loss process (thick line) and calculated Dst* without charge exchange loss process (thin dotted line) are plotted for the period of April 9–25, 1997.*

sufficient decay of ring currents.

3.6. *Energy composition of the plasma pressure*

The differential perpendicular pressure, which is defined as $dP_\perp/dE$ (having a dimension of the number density), is introduced here. Figure 13 shows the calculated differential pressure at different L-values of 4 and 5. The white lines in Fig. 13 indicate the peak energy of the differential perpendicular pressure $dP_\perp/dE$, *i.e.*, ions having the

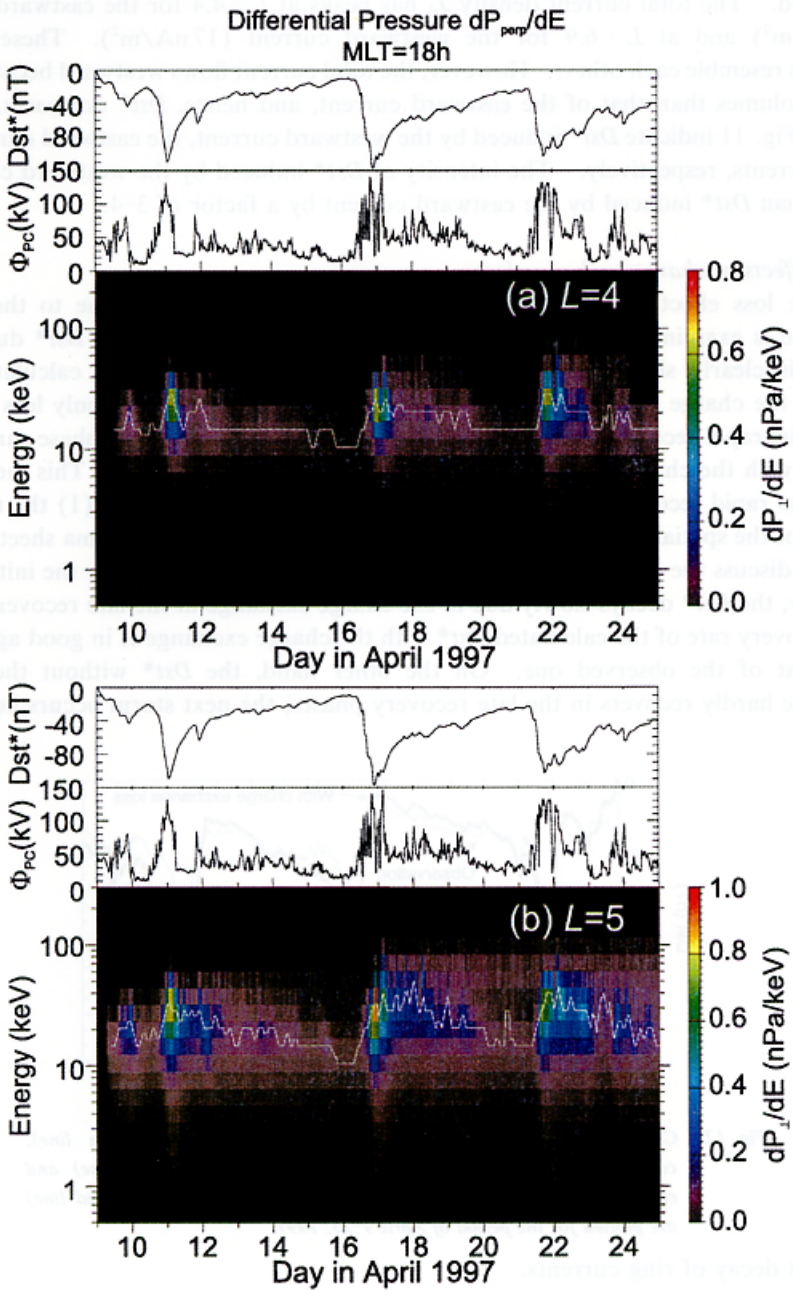

Fig. 13. The differential pressure defined as $dP_{\perp}$ (nPa)/dE (keV) at (a) L=4 and (b) L=5 in cross section at 1800 MLT at 0000 UT on April 16, 1997. White lines indicate a peak of the differential pressure. Each panel shows calculated Dst (top), the polar cap potential Φ_{PC} (middle) and a time series of the differential pressure (bottom).*

energies indicated by the white lines mostly contribute to the perpendicular pressure. The results suggest that the major contributor to the perpendicular plasma pressure is the ions with energies $\simeq$15–30 keV for $L=4$ and $\simeq$30–40 keV for $L=5$–6 during the main phase and the early recovery phase, while the energy of a major contributor is $\simeq$15 keV in the quiet periods. The rise of the major contribution energy to the perpendicular pressure is due to the enhancement of the convection electric field.

The previous satellite observations by the AMPTE/CCE satellite (Active Magnetospheric Particle Tracer Explorer/Charge Composition Explorer) (WILLIAMS, 1985) have shown that there is another peak around 100 keV in the dusk region during the main phase of the large storm on September 5, 1984 when AMPTE/CCE was located between $L=3.7$–4.7 (GLOECKLER *et al.*, 1985). The storm-associated double peaks were also observed by the Explorer 45 satellite (SMITH and HOFFMAN, 1973). The first peak with energies of 15–20 keV observed by AMPTE/CCE is in good agreement with the model calculation, that is, the first peak appears due to the convective transport from the near-earth plasma sheet. However, the second peak (with energy of ~100 keV) is hardly explained by our model. Several processes are proposed to explain the existence of the second peak: (1) CHEN *et al.* (1994) have suggested that substorm-associated temporal electric fields can produce enhancements of the ring current with energies greater than ~100 keV at $L=2.5$–4. (2) ROWLAND and WYGANT (1998) have presented the average structure of the inner magnetospheric electric field directly observed by the CRRES satellite. They observed a noticeable development of the electric field for moderate to high *Kp* at $L=3.5$–6. The intense electric field in the inner magnetosphere is different from the shielded Volland-Stern type electric field. This electric field may push ions with high energies toward the earth (WYGANT *et al.*, 1998). (3) A diffusive process due to the electric and the magnetic field fluctuations is also proposed. For quiet periods, the classical diffusion theory, *e.g.*, DAVIS and CHANG (1962) and NAKADA and MEAD (1965), well explains the real distribution of the high energy particles. However, the diffusive transport processes for active periods are not yet well understood because of the difficulty in determining the diffusion coefficient (*e.g.*, BOSCHER *et al.*, 1998).

3.7. *Response time of the plasma sheet density change to the solar wind*

We have assumed that the plasma sheet density changes with the solar wind density without delay. BOROVSKY *et al.* (1998) have concluded that the response time from the solar wind to the near-earth plasma sheet is of the order of 4 hours. Figure 14 shows the effects of the delay time of the plasma sheet density. The open square, the full square and the full circle indicate the calculated *Dst** without delay time, with delay times of 3 hours and 7 hours, respectively. It is clear from the figure that the calculated *Dst** with the delay time of 7 hours is closer to the observed *Dst** for three storms. It seems reasonable to conclude that the delay time causes a significant change to *Dst** during the main and the early recovery phases. Further analyses and simulations are required to clarify the physical meaning of the estimated delay time.

3.8. *Diamagnetic effect*

A high plasma pressure distorts local magnetic fields; this is called the diamagnetic

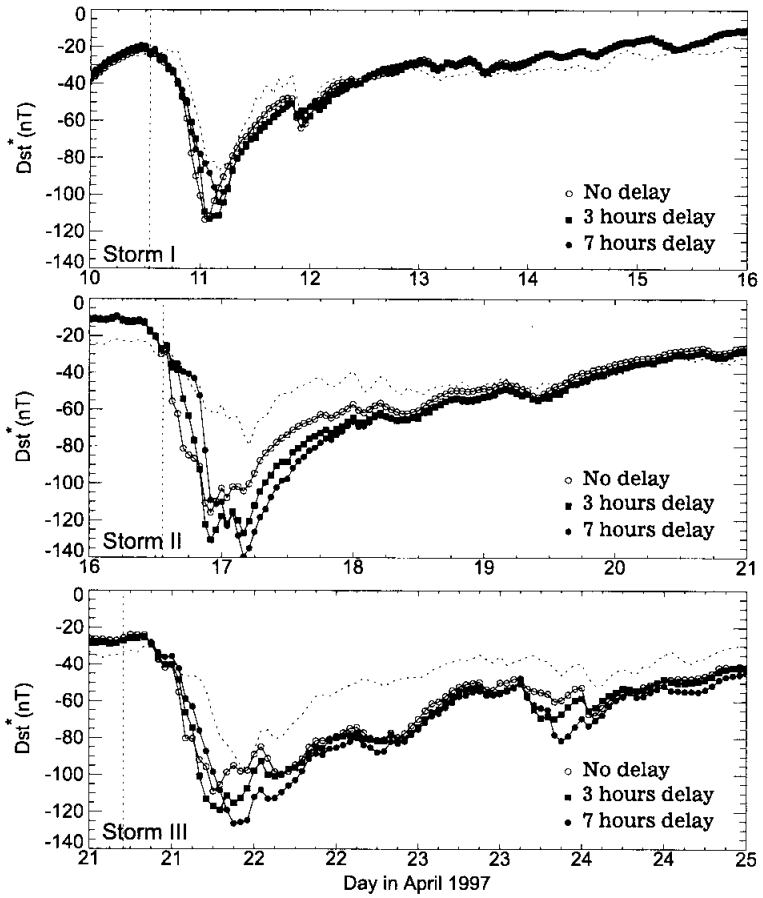

Fig. 14. Effects of the time delay of the plasma sheet density responding to the solar wind density for the three storms ; the top panel for Storm I, the middle panel for Storm II and the bottom panel for Storm III. Three solid lines in a panel indicate calculated Dst with no time delay (open square), with 3 hours delay (full square) and with 7 hours delay (full circle), respectively. A dashed line indicates observed Dst*. A vertical dotted line in all three panels indicates the commencement time of a storm reported by NOAA.*

effect. Such distortion has been observed near the equatorial plane; Explorer 6 (SMITH *et al.*, 1960), Explorer 26 (CAHILL, 1966; HOFFMAN and CAHILL, 1968), Explorer 45 (*e.g.*, CAHILL, 1973), AMPTE/CCE (*e.g.*, POTEMRA *et al.*, 1985), CRRES (WYGANT *et al.*, 1998), ETS-6 (TERADA *et al.*, 1998) and POLAR (TSYGANENKO *et al.*, 1999). It can also be calculated in the present model as shown in Fig. 15.

Figure 15 shows a time series of contour plots of the distorted equatorial magnetic field induced by the ring current during the main and the early recovery phases of the storm on April 10–11, 1997. The distorted field is derived from the Biot-Savart integral

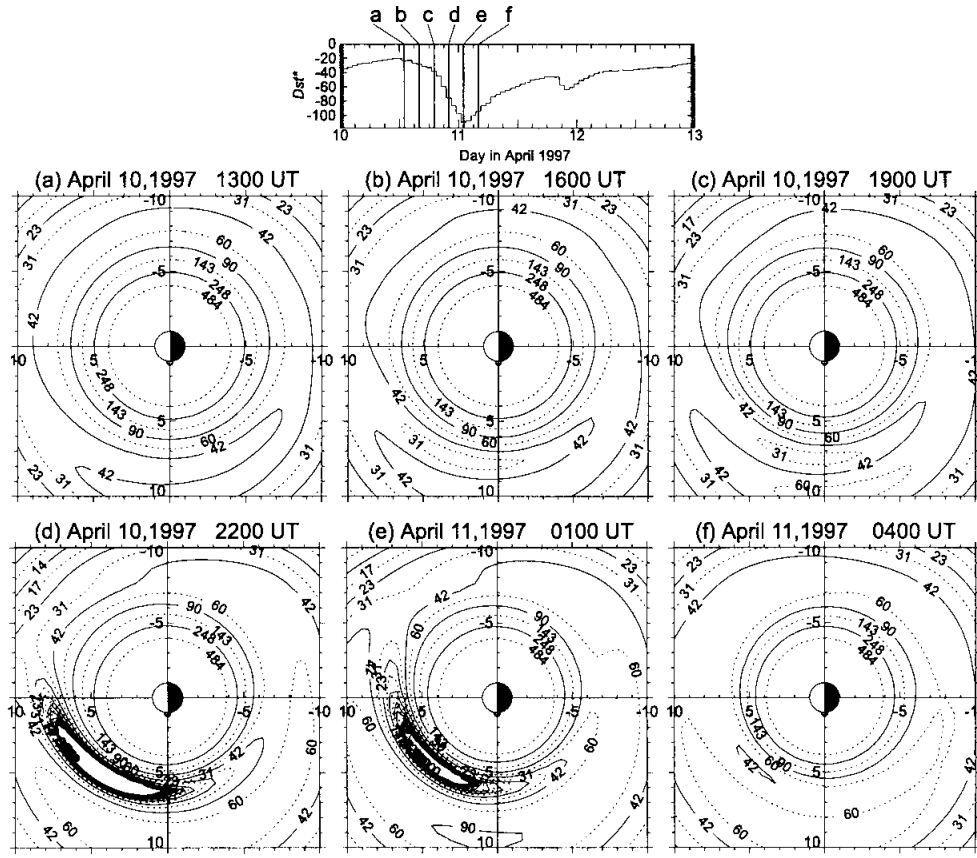

Fig. 15. Distorted equatorial magnetic field due to the ring current. Top panel indicates calculated Dst. Each panel labeled as (a)–(f) shows a contour map of constant equatorial magnetic fields during the main and the early recovery phases of the storm on April 10–11, 1997 at (a) 1300 UT, April 10, 1997 (b) 1600 UT, (c) 1900 UT, (d) 2200 UT, (e) 0100 UT, April 11 and (f) 0400 UT, April 11. Numerical figures written in the contour are the intensity of the magnetic field in nanotesla.*

over the whole three-dimensional distribution of the calculated current; this is the same method as *Dst** is calculated in this study. Note that the ring currents are calculated under the condition of the geomagnetic field to be a given dipole field. This means that our simulation is not self-consistent.

The contour shown in Fig. 15 is a line equivalent to the ∇B drift trajectory. We classified the ∇B drift trajectories into four patterns;

1) an ion drifting westward around the earth (Type 1),
2) an ion drifting westward around the earth but partly drifting eastward in the reversed 'S' shape structure (Type 2),
3) an ion locally drifting anticlockwise around the *magnetic depression*, (Type 3),
4) an ion locally drifting clockwise around the *magnetic hill* (Type 4).

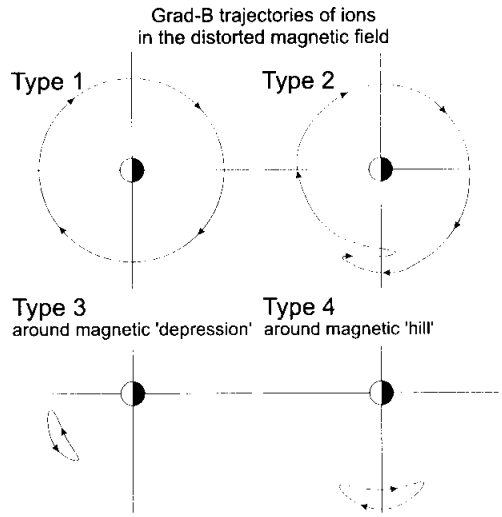

Fig. 16. Schematic ions' ∇B drift trajectories predicted from the calculation. The trajectories are categorized into four patterns (see text).

The trajectories for electrons are opposite to the cases of ions. Type 3 and Type 4 are the trajectories that a particle is locally trapped, never drifting around the earth. These patterns are schematically summarized in Fig. 16.

4. Discussion

The differences between calculated and observed *Dst** are probably attributed to the following reasons.

1) There is an ambiguity of the estimated polar cap potential for given solar wind and IMF conditions. Furthermore, the solar wind and the IMF observed by WIND (located at ~200 Re in April 1997) do not always correspond to those in the vicinity of the earth's magnetosphere. According to the direct observations by CRRES, the storm-time electric field in the inner magnetosphere is different from the Volland-Stern type electric field (ROWLAND and WYGANT, 1998; WYGANT *et al.*, 1998). In future, we will examine the particle motion under the realistic electric field.

2) There is an ambiguity of the estimated plasma sheet density. Discussing this ambiguity is beyond the scope of this paper because the penetration process of the solar wind ions into the magnetosphere is still controversial.

3) High energy ions with energies greater than ~ 100 keV also contribute to the ring current (*e.g.*, SMITH and HOFFMAN, 1973; LUI *et al.*, 1987; HAMILTON *et al.*, 1988; LYONS and SCHULZ, 1989; SHELDON and HAMILTON, 1993). Such high energy ions are steadily trapped by the earth's magnetic field but their trajectories may be changed by the electric and the magnetic field disturbances during a storm. In future, the contribution of such ions to the ring current will be studied to understand the dynamics of the ring current as a whole.

4) This simulation considers no other ion species, *e.g.*, O^+. Energetic O^+ ions become dominate in the inner magnetosphere with the development of magnetic storms. HAMILTON *et al.* (1988), ROEDER *et al.* (1996) and DAGLIS (1997) reported that the energy density of O^+ ions in the ring current often dominates that of H^+ ions in the ring current region during a strong magnetic storm. DAGLIS (1997) has indicated that the energy density of O^+ exceeds that of H^+ during intense magnetic storms with its minimum *Dst* of less than -200 nT, while the energy density of O^+ contributes only to 30% during a moderate magnetic storm (January 2, 1991). According to his analysis, the energy density of O^+ does not always exceed that of H^+ during storms, and the relative amount of O^+ energy density strongly depends on the intensity of *Dst*. The intensity of the minimum *Dst* of the moderate storm reported by DAGLIS (1997) is similar to those of the storms we examined. If the relative amount of O^+ energy density depends on the intensity of *Dst* for all storms, the energy density of O^+ could be a minor contributor to the storm-time energy density in the ring current region for these storms we examined.

5) The induction electric field due to the dipolarization event during the expansion phase of a substorm may change the energy input rate into the ring current. Although the substorm effect to the ring current buildup hardly explains the whole negative variation of storm time *Dst** (*e.g.*, EBIHARA *et al.*, 1998b), minor variations with short time scales of *Dst** could be the result of the substorm effect.

5. Conclusions

1) The major variation of *Dst** is mainly due to the convection electric field and the plasma sheet density. The effectiveness of the solar wind density to the plasma sheet density differs among the storms.

2) The ring current buildup is insensitive to the near-earth plasma sheet temperature for the temperature above 3 keV.

3) *Dst** induced by the westward current is larger than *Dst** induced by the eastward current by a factor of 3–4.

4) The ions with energies of ~15–30 keV at $L=4$, and ~30–40 keV at $L=5$–6 in the dusk region contribute mostly to the perpendicular pressure in the ring current.

5) The previous satellite observations have shown that there is typically another peak with the energy of around 100 keV. This second peak is hardly described by our model. We concluded that further physical processes, an additional electric field or diffusion, are necessary to explain the second peak.

6) The time lag of the plasma sheet density behind the solar wind density causes a significant change to *Dst** during the main and the early recovery phases.

7) The diamagnetic effect by the ring current is greatly enhanced in the equatorial dusk region. The diamagnetic effect will play an important role in both the storm-time ring current buildup and the storm-time redistribution of relativistic particles.

Acknowledgments

We gratefully acknowledge helpful discussions with Prof. T. MUKAI at ISAS and

Prof. T. TERASAWA at University of Tokyo on the relationship between the solar wind and the plasma sheet density. The ion momentum data and the magnetic field data in the plasma sheet are given by the GEOTAIL LEP and MGF instruments, respectively. We would like to thank the PIs for providing their valuable data sets. We used the solar wind and the IMF data sets observed by the MFI and SWE instruments aboard WIND satellite through the ISTP Key Parameters. We are grateful to the PIs, Dr. R. LEPPING and Dr. K. OGILVIE, for the permission to use the data sets. The final *Dst* indices were provided from the WDC-C2 for Geomagnetism, Kyoto University. The NOAA energetic particle data were provided from the WDC-C2 for Aurora, NIPR. The numerical simulations were carried out at Information Science Center (ISC), NIPR.

References

BAUMJOHANN, W. (1996): Near-earth plasma sheet dynamics. Adv. Space Res., **18** (8), 27–33.

BAUMJOHANN, W., PASCHMANN, G. and CATTELL, C.A. (1989): Average plasma properties in the central plasma sheet. J. Geophys. Res., **94**, 6597–6606.

BIRN, J., THOMSEN, M.F., BOROVSKY, J.E., REEVES, G.D., MCCOMAS, D.J. and BELIAN, R.D. (1997): Characteristic plasma properties during dispersionless substorm injections at geosynchronous orbit. J. Geophys. Res., **102**, 2309–2324.

BOROVSKY, J.E., THOMSEN, M.F. and MCCOMAS, D.J. (1997): The superdense plasma sheet: Plasmaspheric origin, solar wind origin, or ionospheric origin? J. Geophys. Res., **102**, 22089–22097.

BOROVSKY, J.E., THOMSEN, M.F. and ELPHIC, R.C. (1998): The driving of the plasma sheet by the solar wind. J. Geophys. Res., **103**, 17617–17639.

BOSCHER, D., BOURDARIE, S., FRIEDEL, R. and KORTH, A. (1998): Long term dynamic radiation belt model for low energy protons. Geophys. Res. Lett., **25**, 4129–4132.

BOURDARIE, S., BOSCHER, D., BEUTIER, T., SAUVAUD, J.-A. and BLANC, M. (1997): Electron and proton radiation belt dynamic simulations during storm periods: A new asymmetric convection-diffusion model. J. Geophys. Res., **102**, 17541–17552.

BOYLE, C.B., REIFF, P.H. and HAIRSTON, M.R. (1997): Empirical polar cap potentials. J. Geophys. Res., **102**, 111–125.

BURTON, R.K., MCPHERRON, R.L. and RUSSELL, C.T. (1975): An empirical relationship between interplanetary conditions and *Dst*. J. Geophys. Res., **80**, 4204–4214.

CAHILL, L.J., Jr. (1966): Inflation of the inner magnetosphere during a magnetic storm. J. Geophys. Res., **71**, 4505–4519.

CAHILL, L.J., Jr. (1973): Magnetic storm inflation in the evening sector. J. Geophys. Res., **78**, 4724–4730.

CHAMBERLAIN, J.W. (1963): Planetary coronae and atmospheric evaporation. Planet. Space Sci., **11**, 901–960.

CHEN, M.W., SCHULZ, M., LYONS, L.R. and GORNEY, D.J. (1993): Stormtime transport of ring current and radiation belt ions. J. Geophys. Res., **98**, 3835–3849.

CHEN, M.W., LYONS, L.R. and SCHULZ, M. (1994): Simulations of phase space distributions of storm time proton ring current. J. Geophys. Res., **99**, 5745–5759.

CHEN, M.W., ROEDER, J.L., FENNELL, J.F., LYONS, L.R. and SCHULZ, M. (1998): Simulations of ring current proton pitch angle distributions. J. Geophys. Res., **103**, 165–178.

CLADIS, J.B. and FRANCIS, W.E. (1985): The polar ionosphere as a source of the storm time ring current. J. Geophys. Res., **90**, 3465–3473.

DAGLIS, I.A. (1997): The role of magnetosphere-ionosphere coupling in magnetic storm dynamics. Magnetic Storms, ed. by B.T. TSURUTANI *et al.* Washington, D.C., Am. Geophys. Union, 107–116 (Geophys. Monogr. Ser., Vol. 98).

DAVIS, L., Jr. and CHANG, D.B. (1962): On the effect of geomagnetic fluctuations on trapped particles. J. Geophys. Res., **67**, 2169–2179.

DELCOURT, D.C., SAUVAND, J.A. and MOORE, T.E. (1990): Cleft contribution to ring current formation. J.

Geophys. Res., **95**, 20937–20943.

DESSLER, A.J. and PARKER, E.N. (1959): Hydrodynamic theory of geomagnetic storms. J. Geophys. Res., **64**, 2239–2252.

EBIHARA, Y. and EJIRI, M. (1998): Modeling of solar wind control of the ring current buildup: A case study of the magnetic storms in April 1997. Geophys. Res. Lett., **25**, 3751–3754.

EBIHARA, Y., EJIRI, M. and MIYAOKA, H. (1998a): Coulomb lifetime of the ring current ions with time varying plasmasphere. Earth Planet. Space, **50**, 371–382.

EBIHARA, Y., EJIRI, M. and MIYAOKA, H. (1998b): Simulation on ring current formation: A case study of a storm on February 13, 1972. Proc. NIPR Symp. Upper Atmos. Phys., **12**, 1–11.

EJIRI, M. (1978): Trajectory traces of charged particles in the magnetosphere. J. Geophys. Res., **83**, 4798–4810.

FOK, M. -C., KOZYRA, J.U., NAGY, A.F., RASMUSSEN, C.E. and KHAZANOV, G.V. (1993): Decay of equatorial ring current ions and associated aeronomical consequences. J. Geophys. Res., **98**, 19381–19393.

FOK, M.-C., MOORE, T.E., KOZYRA, J.U., HO, G.C. and HAMILTON, D.C. (1995): Three-dimensional ring current decay model. J. Geophys. Res., **100**, 9619–9632.

FOK, M.-C., MOORE, T.E. and GREENSPAN, M.E. (1996): Ring current development during storm main phase. J. Geophys. Res., **101**, 15311–15322.

FRANK, L.A. (1967): On the extraterrestrial ring current during geomagnetic storm. J. Geophys. Res., **72**, 3753–3767.

GLOECKLER, G., WILKEN, B., STUDEMANN, W., IPAVICH, F.M., HOVESTADT, D., HAMILTON, D.C. and KREMSER, G. (1985): First composition measurement of the bulk of the storm-time ring current (1 to 300 keV/e) with AMPTE-CCE. Geophys. Res. Lett., **12**, 325–328.

GONZALEZ, W.D., TSURUTANI, B.T., GONZALEZ, A.L.C., SMITH, E.J., TANG, F. and AKASOFU, S.-I. (1989): Solar wind-magnetosphere coupling during intense magnetic storms (1978–1979). J. Geophys. Res., **94**, 8835–8851.

GONZALEZ, W.D., JOSELYN, Y., KAMIDE, H., KROEHL, W., ROSTOKER, G., TSURUTANI, B.T. and VASYLIUNAS, V.M. (1994): What is a geomagnetic storm? J. Geophys. Res., **99**, 5771–5792.

HAMILTON, D.C., GLOECKLER, G., IPAVICH, F.M., STUDEMANN, W., WILKEN, B. and KREMSER, G. (1988): Ring current development during the great geomagnetic storm of February 1986. J. Geophys. Res., **93**, 14343–14355.

HOFFMAN, R.A. and CAHILL, L.J., Jr. (1968): Ring current particle distributions derived from ring current magnetic field measurements. J. Geophys. Res., **73**, 6711–6722.

JANEV, R.K. and SMITH, J.J. (1993): Cross sections for collision processes of hydrogen atoms with electrons, protons, and multipli-charged ions. Atomic and Plasma-Material Interaction Data for Fusion. IAEA, **4**, 78–79.

JORDANOVA, V.K., KOZYRA, J.U., KHAZANOV, G.V., NAGY, A.F., RASMUSSEN, C.E. and FOK, M.-C. (1994): A bounce-averaged kinetic model of the ring current ion population. Geophys. Res. Lett., **21**, 2785–2788.

JORDANOVA, V.K., FARRUGIA, C.J., JANOO, L., QUINN, J.M., TORBERT, R.B., OGILVIE, K.W., LEPPING, R.P., STEINBERG, J.T., MCCOMAS, D.J. and BELIAN, R.D. (1998): October 1995 magnetic cloud and accompanying storm activity: Ring current evolution. J. Geophys. Res., **103**, 79–92.

KAMIDE, Y. and FUKUSHIMA, N. (1971) Analysis of magnetic storms with DR-indices for equatorial ring current field. Rep. Ionos. Space Res. Jpn., **25**, 125–162.

KISTLER, L.M., IPAVICH, F.M., HAMILTON, D.C., GLOECKLER, G., WILKEN, B., KREMSER, G. and STUDEMANN, W. (1989): Energy spectra of the major ion species in the ring current during geomagnetic storms. J. Geophys. Res., **94**, 3579–3599.

KOKUBUN, S., YAMAMOTO, T., ACUNA, M.H., HAYASHI, K., SHIOKAWA, K. and KAWANO, H. (1994): The Geotail magnetic field experiment. J. Geomag. Geoelectr., **46**, 7–21.

KOZYRA, J.U., FOK, M.-C., SANCHEZ, E.R., EVANS, D.S., HAMILTON, D.C. and NAGY, A.F. (1998a): The role of precipitation losses in producing the rapid early recovery phase of the Great Magnetic Storm of February 1986. J. Geophys. Res., **103**, 6801–6814.

KOZYRA, J.U., JORDANOVA, V.K., BOROVSKY, J.E., THOMSEN, M.F., KNIPP, D.J., EVANS, D.S., MCCOMAS, D. J. and CAYTON, T.E. (1998b): Effects of a high-density plasma sheet on ring current development

during the November 2–6, 1993, magnetic storm. J. Geophys. Res., **103**, 26285–26305.

LEE, L.C., CORRICK, G. and AKASOFU, S.-I. (1983): On the ring current energy injection rate. Planet. Space Sci., **31**, 901–911.

LEPPING, R.P., ACUNA, M., BURLAGA, L., FARRELL, W., SLAVIN, J., SCHATTEN, K., MARIANI, F., NESS, N., NEUBAUER, F., WHANG, Y.C., BYRNES, J., KENNON, R., PANETTA, P., SCHEIFELE, J. and WORLEY, E. (1995): The wind magnetic field investigation. Space Sci. Rev., **71**, 207–229.

LUI, A.T.Y. (1993): Radial transport of storm time ring current ions. J. Geophys. Res., **98**, 209–214.

LUI, A.T.Y., MCENTIRE, R.W. and KRIMIGIS, S.M. (1987): Evolution of the ring current during two geomagnetic storms. J. Geophys. Res., **92**, 7459–7470.

LYONS, L.R. and EVANS, D.S. (1976): The inconsistency between proton charge exchange and the observed ring current decay. J. Geophys. Res., **81**, 6197–6200.

LYONS, L.R. and SCHULZ, M. (1989): Access of energetic particles to storm time ring current through enhanced radial "diffusion". J. Geophys. Res., **94**, 5491–5496.

LYONS, L.R. and WILLIAMS, D.J. (1980): A source for the geomagnetic storm main phase ring current. J. Geophys. Res., **85**, 523–530.

MAKITA, K., MENG, C.-I. and AKASOFU, S.-I. (1983): The shift of the auroral electron precipitation boundaries in the dawn-dusk sector in association with geomagnetic activity and interplanetary magnetic field. J. Geophys. Res., **88**, 7967–7981.

MAYNARD, N.C. and CHEN, A.J. (1975): Isolated cold plasma regions: observations and their relation to possible production mechanisms. J. Geophys. Res., **80**, 1009–1013.

MUKAI, T., MACHIDA, S., SAITO, Y., HIRAHARA, M., TERASAWA, T., KAYA, N., OBARA, T., EJIRI, M. and NISHIDA, A. (1994): The low energy particle (LEP) experiment onboard the GEOTAIL satellite. J. Geomag. Geoelectr., **46**, 669–692.

NAKADA, M.P. and MEAD, G.D. (1965): Diffusion of protons in the outer radiation belt. J. Geophys. Res., **70**, 4777–4791.

NOËL, S. (1997): Decay of the magnetospheric ring current: A Monte Carlo simulation. J. Geophys. Res., **102**, 2301–2308.

NORTHROP, T.G. (1963): The adiabatic motion of charged particles. New York, Interscience publishers.

OGILVIE, K.W., CHORNEY, D.J., FITZENREITER, R.J., HUNSAKER, F., KELLER, J., LOBELL, J., MILLER, G., SCUDDER, J.D., SITTLER, E.C., Jr., TORBERT, R.B., BODET, D., NEEDELL, G., LAZARUS, A.J., STEINBERG, J.T., TAPPAN, J.H., MAVRETIC, A. and GERGIN, E. (1995): SWE, a comprehensive plasma instrument for the Wind spacecraft. Space Sci. Rev., **71**, 55–77.

PARKER, E.N. (1957): Newtonian Development of the dynamical properties of ionized gases of low density. Phys. Rev., **107**, 924–933.

PARKS, G.K., LIN, C.S., MAUK, B., DEFOREST, S. and MCILWAIN, C.E. (1977): Characteristics of magnetospheric particle injection deduced from events observed on August 18, 1974. J. Geophys. Res., **82**, 5208–5214.

PATERSON, W.R., FRANK, L.A., KOKUBUN, S. and YAMAMOTO, T. (1998): Geotail survey of ion flow in the plasma sheet: Observations between 10 and 50 Re. J. Geophys. Res., **103**, 11811–11825.

PEROOMIAN, V. and ASHOUR-ABDALLA, M. (1996): Population of the near-earth magnetotail from the auroral zone. J. Geophys. Res., **101**, 15387–15401.

POTEMRA, T.A., ZANETTI, L.J. and ACUNA, M.H. (1985): AMPTE/CCE magnetic field studies of the September 4, 1984 storm. Geophys. Res. Lett., **12**, 313–316.

PRÜLSS, G.W. (1973): Decay of the magnetic storm ring current by the charge-exchange mechanism. Planet. Space Sci., **21**, 983–992.

RAIRDEN, R.L, FRANK, L.A. and CRAVEN, J.D. (1986): Geocoronal imaging with Dynamics Explorer. J. Geophys. Res., **91**, 13613–13630.

RILEY, P. and WOLF, R.A. (1992): Comparison of diffusion and particle drift descriptions of radial transport in the earth's inner magnetosphere. J. Geophys. Res., **97**, 16865–16876.

ROEDER, J.L., FENNELL, J.F., CHEN, M.W., GRANDE, M., LIVI, S. and SCHULZ, M. (1996): CRRES observations of stormtime ring current ion composition. AIP Conf. Proc., Workshop on the Earth's Trapped Particle Environment, no. 383, 131–135.

ROEDERER, J.G. (1970): Dynamics of Geomagnetically Ttrapped Rradiation. Berlin, Springer.

ROWLAND, D.E. and WYGANT, J.R. (1998): Dependence of the large-scale, inner magnetospheric electric field on geomagnetic activity. J. Geophys. Res., **103**, 14959–14964.

SCKOPKE, N. (1966): A general relation between the energy of trapped particles and the disturbance field near the earth. J. Geophys. Res., **71**, 3125–3130.

SHELDON, R.B. and HAMILTON, D.C. (1993): Ion transport and loss in the earth's quiet ring current. 1. Data and standard model. J. Geophys. Res., **98**, 13491–13508.

SHELLEY, E.G., JOHNSON, R.G. and SHARP, R.D. (1972): Satellite observations of energetic heavy ions during a geomagnetic storm. J. Geophys. Res., **77**, 6104–6110.

SHELLEY, E.G., SHARP, R.D. and JOHNSON, R.G. (1976): Satellite observations of an ionospheric acceleration mechanism. Geophys. Res. Lett., **3**, 654–656.

SHUKHTINA, M.A. (1993): On the calculation of the magnetic drift velocity of particles with arbitrary pitch angles. Planet. Space Sci., **41**, 327–331.

SMITH, P.H. and BEWTRA, N.K. (1978): Charge exchange lifetimes for ring current ions. Space Sci. Rev., **22**, 301–318.

SMITH, P.H. and HOFFMAN, R.A. (1973): Ring current particle distributions during the magnetic storms of 16 -18 December 1971. J. Geophys. Res., **78**, 4731–4737.

SMITH, E.J., COLEMAN, P.J., JUDGE, D.L. and SONETT, C.P. (1960): Characteristics of the extraterrestrial current system: Explorer VI and Pioneer V. J. Geophys. Res., **65**, 1958–1861.

SMITH, P.H., HOFFMAN, R.A. and FRITZ, T.A. (1976): Ring current proton decay by charge exchange, J. Geophys. Res., **81**, 2701–2708.

SMITH, P.H., BEWTRA, N.K. and HOFFMAN, R.A. (1981): Inference of the ring current ion composition by means of charge exchange decay. J. Geophys. Res., **86**, 3470–3480.

STERN, D.P. (1975): The motion of a proton in the equatorial magnetosphere. J. Geophys. Res., **80**, 595–599.

SWISHER, R.L. and FRANK, L.A. (1968): Lifetimes for low-energy protons in the outer radiation zone. J. Geophys. Res., **73**, 5655–5672.

TAKAHASHI, S., IYEMORI, T. and TAKEDA, M. (1990): A simulation of the storm-time ring current. Planet. Space Sci., **38**, 1133–1141.

TERADA, N., IYEMORI, T. NOSE, M., NAGAI, T., MATSUMOTO, H. and GOKA, T. (1998): Storm-time magnetic field variations observed by the ETS-VI satellite. Earth Planet. Space, **50**, 853–864.

TERASAWA, T., FUJIMOTO, M., MUKAI, T., SHINOHARA, I., SAITO, Y., YAMAMOTO, T., MACHIDA, S., KOKUBUN, S., LAZARUS, A.J., STENBERG, J.T. and LEPPING, R.P. (1997): Solar wind control of density and temperature in the near-earth plasma sheet: WIND/GEOTAIL collaboration. Geophys. Res. Lett., **24**, 935–938.

THOMSEN, M.F., BOROVSKY, J.E., MCCOMAS, D.J. and COLLIER, M.R. (1998): Variability of the ring current source population. Geophys. Res. Lett., **25**, 3481–3484.

TINSLEY, B.A. (1976): Evidence that the recovery phase ring current consists of helium ions. J. Geophys. Res., **81**, 6193–6195.

TSYGANENKO, N.A., LE, G., RUSSELL, C.T. and IYEMORI, T. (1999): A study of the inner magnetosphere based on data of Polar. J. Geophys. Res., **104**, 10275–10284.

VOLLAND, H. (1973): A semiempirical model of large-scale magnetospheric electric fields. J. Geophys. Res., **78**, 171–181.

WILLIAMS, D.J. (1981): Ring current composition and sources: An update. Planet. Space Sci., **29**, 1195–1203.

WILLIAMS, D.J. (1985): Exploration and understanding in space physics. Geophys. Res. Lett., **12**, 303–308.

WODNICKA, E.B. (1989): The magnetic storm main phase modeling. Planet. Space Sci., **37**, 525–534.

WOLF, R.A., FREEMAN, J.W., Jr., HAUSMAN, B.A., SPIRO, R.W., HILMER, R.V. and LAMBOR, R.L. (1997): Modeling convection effects in magnetic storms. Magnetic Storms, ed. by B.T. TSURUTANI *et al.* Washington, D.C., Am. Geophys. Union, 161–172 (Geophys. Monogr. Ser., Vol. 98).

WYGANT, J., ROWLAND, D., SINGER, H.J., TEMERIN, M., MOZER, F. and HUDSON, M.K. (1998): Experimental evidence on the role of the large spatial scale electric field in creating the ring current. J. Geophys. Res., **103**, 29527–29544.

(Received February 2, 1999; Revised manuscript accepted April 15, 1999)

Appendix A: Model Calculation

A1. Particles' motion

The motion of energetic charged particles in the dipolar magnetic field is a superposition of three periodic motions; gyration about the local magnetic field line, bouncing between the northern and southern hemispheres along the field line and drifting perpendicular to the field line. Many computer resources are, in general, required to solve the Lorentz equation that governs the complete particle motion.

If the temporal variation of the electromagnetic fields for a gyroperiod is negligible, motion of a particle can be approximated by motion of its guiding center (NORTHROP, 1963). Averaging over the bouncing motion between mirror points, the guiding center motion can be projected onto an equatorial plane if the configuration of the magnetic field is a dipole or particular cases (*e.g.*, ROEDERER, 1970; SHUKHTINA, 1993). The bounce-averaged drift velocity $<V_s>$ under the dipolar magnetic field is given by

$$<V_s> = \frac{E \times B}{B^2} + \frac{WG(\alpha_0)}{qB^3} B \times \nabla B, \tag{A1}$$

where B is the magnetic field, E the electric field, W the kinetic energy, α_0 the equatorial pitch angle and q the charge. The function of G (α_0) is given by EJIRI (1978).

The bounce-averaged drift trajectories under the dipole magnetic field and the Volland-Stern type convection field can be obtained by solving the following equations (EJIRI, 1978) as

$$\frac{dX}{dt} = -\frac{\omega}{\gamma} X^{\gamma+2} \cos\phi, \tag{A2}$$

$$\frac{d\phi}{dt} = \omega X^{\gamma+1} \sin\phi + \omega - \frac{3\mu G(y_0)}{qR_s^2 X^2}, \tag{A3}$$

$$\frac{dy_0}{dt} = -\frac{y_0 I(y_0)}{4f(y_0)} \frac{1}{X} \frac{dX}{dt}, \tag{A4}$$

$$X = \frac{R}{R_s}, \tag{A5}$$

where ω is the angular velocity of the earth's rotation, ϕ the local time, γ the shielding factor of the convection field, y_0 the sine of the equatorial pitch angle, I (y_0) a function related to the second invariant, μ the first adiabatic invariant (magnetic moment) and R_s is the geocentric distance of a stagnation point at 1800 MLT for a zero energy particle. The geocentric distance of a stagnation point (R_s) for a zero energy particle is

$$R_s = \left(\frac{\omega R e^3 B_0}{A\gamma} \right)^{\frac{1}{\gamma+1}}. \tag{A6}$$

The function $I(y_0)$ is given by

$$I = \frac{1}{R} \int_{s_1}^{s_2} \left[1 - \frac{B(s)}{B_m} \right]^{1/2} ds, \tag{A7}$$

where B_m is the intensity of the magnetic field at the mirror points s_1 and s_2.

Solving the equations, eq. (A2), eq. (A3) and eq. (A4), one can trace the bounce-averaged drift trajectory for a given initial condition. Several proton and electron bounce-averaged trajectories are illustrated in Figs. A1 and A2.

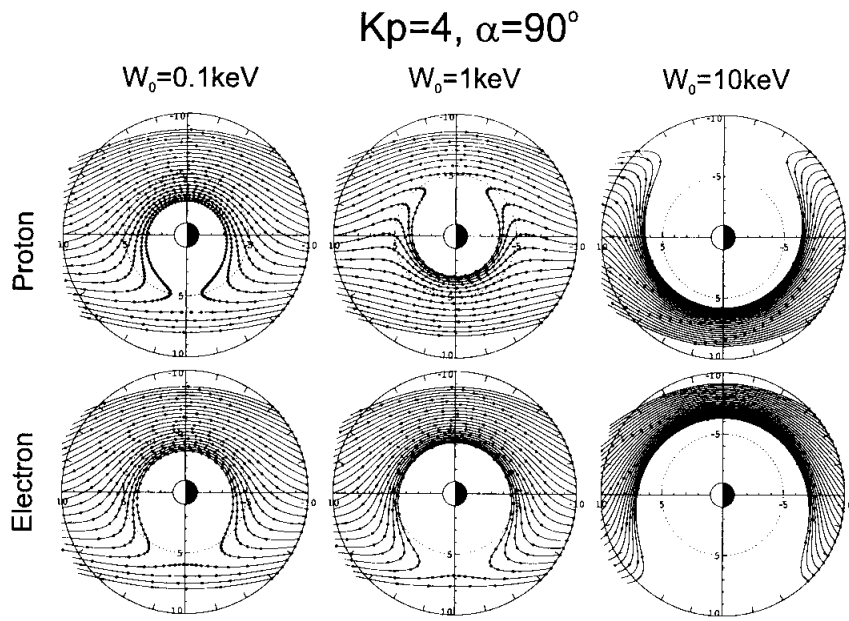

Fig. A 1. Magnetic moment dependence of bounce-averaged trajectories for protons (top panels) and electrons (bottom panels) with their pitch angles of 90°. From left to right panels, each panel indicates the trajectories for the initial kinetic energies of 0.1, 1, and 10 keV, respectively. They correspond to the magnetic moments of 3.23 eV/nT, 32.3 eV/nT and 323 eV/nT, respectively. The trajectories are traced under the dipole magnetic field and the Volland-Stern type convection field with its intensity for Kp=4 case by the MAYNARD *and* CHEN *(1975) model. All particles start at L=10. Particle positions are represented by dots at 10-minute steps.*

A2. Differential flux and macroscopic quantities

Following CLADIS and FRANCIS (1985), we derived a method to calculate the absolute differential flux of the trapped particles. A basic concept for the derivation is that a packet particle carries a number of real particles in a small phase space bin; this is conceptually corresponding to the Liouville theorem.

A directional differential flux j is defined as

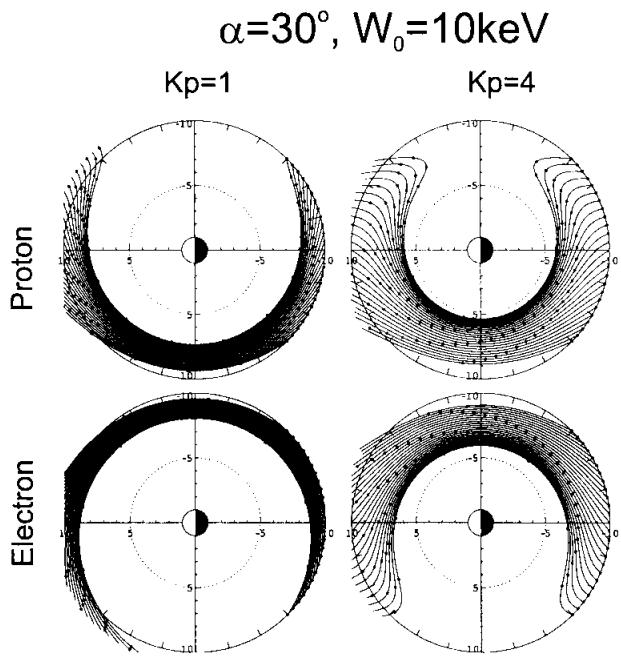

Fig. A 2. Same as previous figure except that the intensity of the convection field dependence of the bounce-averaged trajectories for protons (top panels) and electrons (bottom panels) with their pitch angles of 30° and the initial kinetic energy of 10 keV (323 eV/nT). Left panels indicate the trajectories for Kp = 1 and bottom panels for Kp = 4.

$$j = \frac{\mathrm{d}N}{\mathrm{d}S_{\perp}\,\mathrm{d}t\mathrm{d}\Omega\mathrm{d}W}\,, \tag{A8}$$

where $\mathrm{d}S_{\perp}$ and Ω are the area of a (virtual) detector and the solid angle, respectively. $\mathrm{d}N$ is a number of particles that flow through the detector per unit perpendicular area. The directional differential flux whose detector is placed in the equatorial plane gives a three-dimensional distribution of the differential flux because all particles pass through the equatorial plane except for particles with their pitch angles within a loss cone. The differential flux in the equatorial plane j_0 is given by

$$j_0 = \frac{\mathrm{d}N}{2\pi\mathrm{d}S\tau_{\mathrm{b}}(y_0)y_0\,\mathrm{d}y_0\,\mathrm{d}W}\,, \tag{A9}$$

where τ_{b} is the bounce period. Here the sine of the equatorial pitch angle (y_0) is introduced instead of the solid angle (Ω).

Assuming that the magnetic flux is conserved and that the total kinetic energy and

the magnetic moment of particles are conserved, the off-equatorial flux j at a latitude of λ can be derived from the Liouville theorem (ROEDERER, 1970) as

$$j(y) = j_0(y_0), \tag{A10}$$

with

$$y_0 = y \frac{\cos^3 \lambda}{(1+3\sin^2 \lambda)^{1/4}} . \tag{A11}$$

The perpendicular pressure $P_\perp$ and the parallel plasma pressure $P_\parallel$ are given by

$$P_\perp = \int m v^2 F(v) \cos^2 \alpha \mathrm{d}v, \tag{A12}$$

$$P_\parallel = \int \frac{1}{2} m v^2 F(v) \sin^2 \alpha \mathrm{d}v, \tag{A13}$$

where F is the velocity distribution function and m the particle's mass. The pressure can be expressed by using the directional differential flux j instead of the velocity distribution function F, as

$$P_\perp = \pi \sqrt{2m} \int_\alpha \int_W j \sqrt{W} \sin^3 \alpha \mathrm{d}\alpha \mathrm{d}W, \tag{A14}$$

$$P_\parallel = 2\pi \sqrt{2m} \int_\alpha \int_W j \sqrt{W} \cos^2 \alpha \sin \alpha \mathrm{d}\alpha \mathrm{d}W. \tag{A15}$$

The current density perpendicular to the magnetic field in the ring current has been considered as a combination of the three currents (PARKER, 1957); the magnetization current J_M, the curvature drift current J_R and the grad-B drift current J_B. The polarization current and the gravitational current are neglected here. The magnetization current is due to particles' gyration and is expressed as

$$\boldsymbol{J}_M = \nabla \times \boldsymbol{M}, \tag{A16}$$

with

$$\boldsymbol{M} = -\frac{P_\perp \boldsymbol{B}}{\boldsymbol{B}^2}. \tag{A17}$$

The drift currents, J_R and J_B, are

$$\boldsymbol{J}_R = \frac{P_\parallel}{\boldsymbol{B}^4} \boldsymbol{B} \times (\boldsymbol{B} \cdot \nabla) \boldsymbol{B}, \tag{A18}$$

and

$$\boldsymbol{J}_{\mathrm{B}}=\frac{P_{\perp}}{B^3}\boldsymbol{B}\times\nabla B, \tag{A19}$$

respectively. Thus the total azimuthal current density $\boldsymbol{J}_{\perp}$ is

$$\begin{aligned}\boldsymbol{J}_{\perp}&=\boldsymbol{J}_{\mathrm{M}}+\boldsymbol{J}_{\mathrm{R}}+\boldsymbol{J}_{\mathrm{B}}\\&=\frac{\boldsymbol{B}}{B^2}\times\left[\nabla P_{\perp}+(P_{\perp}-P_{\parallel})\frac{(\boldsymbol{B}\cdot\nabla)\boldsymbol{B}}{B^2}\right].\end{aligned} \tag{A20}$$

In the dipolar magnetic field, three components of the current density, the radial component (J_r), the azimuthal component positive eastward (J_ϕ) and the latitudinal component (J_λ), become

$$\begin{aligned}J_r(r,\phi,\lambda)&=-\frac{B_\lambda}{B^2 r\cos\lambda}\frac{\partial P_{\perp}}{\partial\phi}\\&=-\frac{r^2}{M(1+3\sin^2\lambda)}\frac{\partial P_{\perp}}{\partial\phi},\end{aligned} \tag{A21}$$

$$\begin{aligned}J_\phi(r,\phi,\lambda)&=\frac{1}{B^2}\left(\frac{B_r}{r}\frac{\partial P_{\perp}}{\partial\lambda}-B_\lambda\frac{\partial P_{\perp}}{\partial r}\right)\\&\quad+\frac{1}{B^3}(P_{\parallel}-P_{\perp})\left(\frac{B_r}{r}\frac{\partial B}{\partial\lambda}-B_\lambda\frac{\partial B}{\partial r}\right)\end{aligned} \tag{A22}$$

$$\begin{aligned}&=\frac{r^3}{M(1+3\sin^2\lambda)}\\&\quad\left[-\frac{2}{r}\sin\lambda\frac{\partial P_{\perp}}{\partial\lambda}-\cos\lambda\frac{\partial P_{\perp}}{\partial r}\right.\\&\quad\left.+\frac{P_{\perp}-P_{\perp}}{r}\left(-\frac{6\sin^2\lambda\cos\lambda}{1+3\sin^2\lambda}+3\cos\lambda\right)\right],\end{aligned} \tag{A23}$$

$$\begin{aligned}J_\lambda(r,\phi,\lambda)&=-\frac{B_r}{B^2 r\cos\lambda}\frac{\partial P_{\perp}}{\partial\phi}\\&=-\frac{r^2\sin\lambda}{M(1+3\sin^2\lambda)\cos\lambda}\frac{\partial P_{\perp}}{\partial\phi},\end{aligned} \tag{A24}$$

where B_r is the radial component of the magnetic field, B_λ the latitudinal component of the magnetic field, r the radial distance from the center of the earth and M the magnetic moment of the earth.

By integrating the three-dimensional distribution of the current density, the magnetic disturbance at the geocentric distance of r can be derived from the Biot-Savart law as

$$\Delta\boldsymbol{B}(r)=\frac{\mu_0}{4\pi}\int\frac{\boldsymbol{J}_{\perp}(\boldsymbol{r}')\times(\boldsymbol{r}-\boldsymbol{r}')}{|\boldsymbol{r}-\boldsymbol{r}'|^3}\mathrm{d}^3\boldsymbol{r}', \tag{A25}$$

where μ_0 is the permeability in vacuum. Especially, the magnetic disturbance parallel

to the earth's dipole at the center of the earth ΔB_C is given by

$$\Delta B_C = \frac{\mu_0}{4\pi} \int_r \int_\lambda \int_\phi \cos\lambda J_\phi(r,\lambda,\phi) \mathrm{d}r \mathrm{d}\lambda \mathrm{d}\phi. \tag{A26}$$

Appendix B: Derivation of the Energy Input Rate into the Ring Current

The total energy Γ injected from the near-earth plasma sheet through the 'injection boundary' is defined as

$$\Gamma \equiv \int \frac{1}{2} m v^2 F(v) \mathrm{d}x \mathrm{d}v \tag{B1}$$

$$= \int \frac{1}{2} m v^2 F(v) \mathrm{d}S v \mathrm{d}t \cos\alpha v^2 \mathrm{d}\Omega \mathrm{d}v$$

$$= 2\pi m \int \mathrm{d}S \int F(v) v^4 S_b(y) y \mathrm{d}y \mathrm{d}v, \tag{B2}$$

where $F(v)$ is the velocity distribution function, m the mass, S the area, α the pitch angle, y the sine of a pitch angle, τ_b the bounce period and $S_b(y)$ is

$$\tau_b = \frac{2}{v} \int \left(1 - \frac{B_m}{B}\right)^{1/2} \mathrm{d}s \tag{B3}$$

$$\equiv \frac{2}{v} S_b(y), \tag{B4}$$

where B_m and $\mathrm{d}s$ are the magnetic field at a mirror point, the line element along with a field line, respectively.

Since the velocity distribution function at the 'injection boundary' is assumed to be isotropic and Maxwellian in this simulation, the velocity distribution function F becomes

$$F = \frac{N_{ps}}{(\pi v_0^2)^{3/2}} \exp\left(-\frac{v^2}{v_0^2}\right), \tag{B5}$$

where N_{ps} and v_0 are the number density in the plasma sheet and the most probable velocity, respectively.

In polar coordinates, the area $\mathrm{d}S$ in the equatorial plane is given by

$$\mathrm{d}S = R_0 \mathrm{d}\phi \mathrm{d}R$$

$$= R_0 \mathrm{d}\phi \mathrm{d}t \frac{\mathrm{d}R}{\mathrm{d}t}$$

$$= R_0 \mathrm{d}\phi \mathrm{d}t \frac{E_\phi}{B}, \tag{B6}$$

where R_0, ϕ and E_ϕ are the geocentric distance of the 'injection boundary', the local time and the azimuthal component of the electric field, respectively. If the convection field is expressed by the Volland-Stern type, the azimuthal component of the electric field is

easily obtained as

$$E_\phi = -\frac{1}{R}\frac{\partial \Phi}{\partial \phi} \tag{B7}$$

$$= -AR\cos -\phi, \tag{B8}$$

$$A = \frac{\Phi_{PC}}{2R_B{}^2}, \tag{B9}$$

where Φ, R_B and Φ_{PC} are the electric potential, the geocentric distance of the magnetopause and the polar cap potential, respectively. Then the area dS becomes

$$dS = \frac{\Phi_{PC}}{2B}\left(\frac{R_0}{R_B}\right)^2 dt \cos\phi d\phi. \tag{B10}$$

After substituting eq. (B5), eq. (B6) and eq. (B10) into eq. (B2), the total energy Γ is given by

$$\Gamma = \frac{3}{2} N_{ps} E_0 \frac{\Phi_{PC}}{2B}\left(\frac{R_0}{R_B}\right)^2 \int dt \int \cos\phi \, d\phi \int S_b y dy,$$

where E_0 is the temperature corresponding to $mv_0{}^2/2$. Now, the energy input rate γ is introduced as

$$\gamma = \Gamma / \int dt$$

$$= \frac{3N_{ps}E_0\,\Phi_{PC}}{4B}\left(\frac{R_0}{R_B}\right)^2 Y(R) \int \cos\phi \, d\phi \text{ (watt)}, \tag{B11}$$

$$Y(R_0) \equiv \int S_b(y) y dy. \tag{B12}$$

After substituting R_0 of 10 Re, ϕ of 21 h–3 h (27 h) and R_B of 10.47 Re, which are used in this simulation, into eq. (B11), the energy input rate γ becomes

$$\gamma = 0.572 N_{ps}(\text{cm}^{-3}) E_0(\text{keV}) \Phi_{PC}(\text{kV}) \text{ (gigawatt)}. \tag{B13}$$

Appendix C: Bounce Periods and Drift Periods

A bounce period of a magnetically trapped particle in a dipole magnetic field is given by

$$\tau_b = \frac{2}{v}\int \left(1 - \frac{B_m}{B}\right)^{1/2} ds, \tag{C1}$$

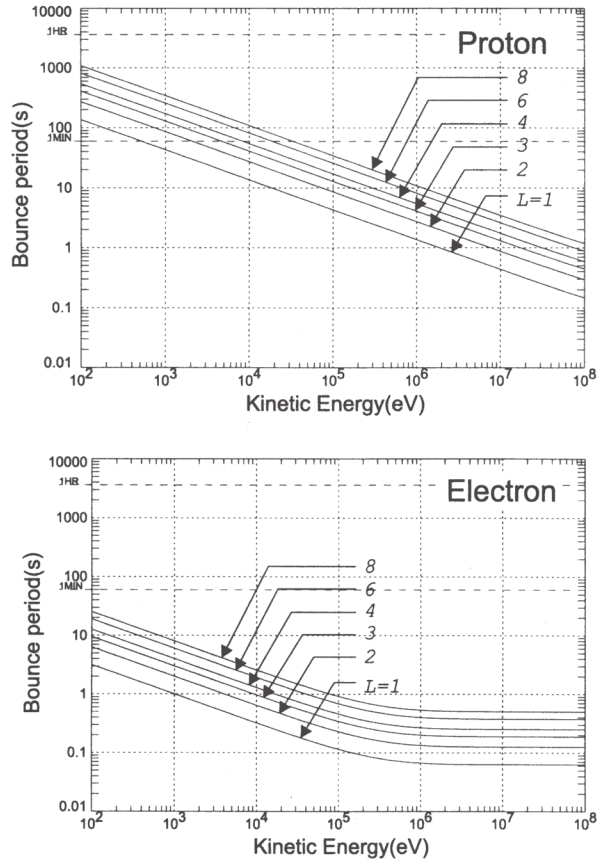

Fig. A 3. Bounce periods of trapped protons (top) and electrons (bottom) as a function of kinetic energy. Six lines indicate the periods at L=1, 2, 3, 4, 6 and 8, respectively.

where B is the magnetic field intensity, B_m the magnetic field intensity at a mirror point, ds the line element along a field line, v the particle's speed. The bounce periods of particles with their pitch angles of 90° as a function of a kinetic energy and L are shown in Fig. A3.

In a dipole magnetic field, a grad-B drift velocity of a trapped particle in the equatorial plane is given by

$$V_{\nabla B} = \frac{mv^2}{2qB^2} \, |\nabla_{\perp} B| \, , \tag{C2}$$

where m and q are the particle's mass and the charge, respectively. Thus the drift period of a particle with its equatorial pitch angle of 90° becomes

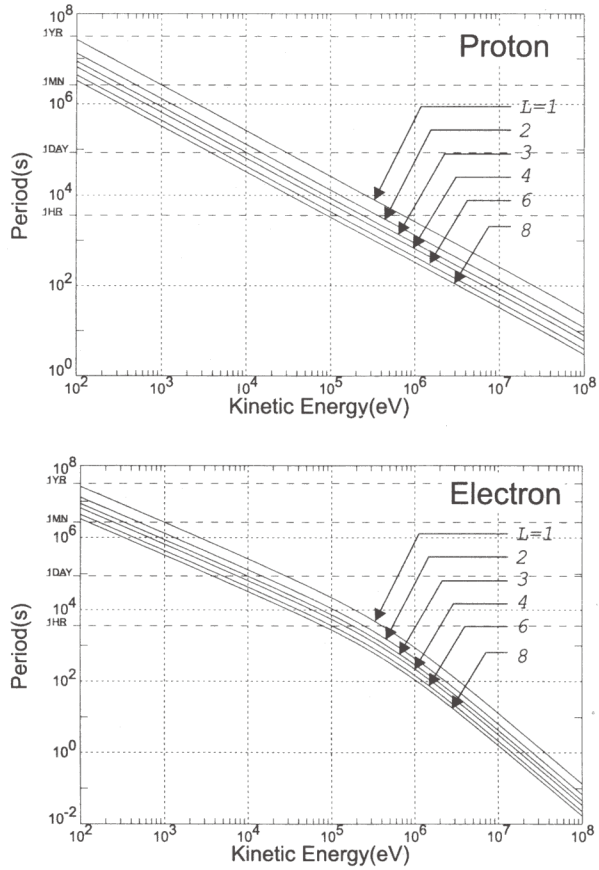

Fig. A 4. Drift periods of trapped protons (top) and electrons (bottom) as a function of kinetic energy due to the grad-B drift. The $E \times B$ drift is excluded. Six lines indicate the periods at $L=1$, 2, 3, 4, 6 and 8, respectively.

$$\tau_{\nabla B} = \frac{2\pi r}{V_{\nabla B}}, \tag{C3}$$

where r is the geocentric distance. The drift periods of the particles are shown in Fig. A4.

The bounce periods and the drift periods at $L=3$, 4, 5, 6, 7 and 8 are listed in Table A1 with gyroperiods and gyroradii.

Table A 1. Gyroperiod, bounce period, drift period and gyroradius of a trapped particle with a pitch angle of 90° at L=3, 4, 5, 6, 7 and 8 for kinetic energies (E) of 1, 10, 100 and 1000 keV in the equatorial plane.

	E (keV)	gyroperiod (s)	bouncing period (s)	drift period (hour)	gyroradius (km)
		$L=3$, $\alpha_0=90°$			
Protons	1.0	5.713×10^{-2}	129.3	244.0	3.98
	10.0	5.713×10^{-2}	40.87	24.4	12.59
	100.0	5.714×10^{-2}	12.93	2.44	39.8
	1000.0	5.719×10^{-2}	4.091	0.2441	125.9
Electrons	1.0	3.118×10^{-5}	3.021	244.3	0.09292
	10.0	3.172×10^{-5}	0.9678	24.64	0.2951
	100.0	3.720×10^{-5}	0.3442	2.658	0.9731
	1000.0	9.200×10^{-5}	0.2005	0.3647	4.131
		$L=4$, $\alpha_0=90°$			
	E (keV)	gyroperiod (s)	bouncing period (s)	drift period (hour)	gyroradius (km)
Protons	1.0	0.1354	172.3	183.0	9.434
	10.0	0.1354	54.50	18.3	29.83
	100.0	0.1354	17.24	1.83	94.34
	1000.0	0.1356	5.454	0.1831	298.4
Electrons	1.0	7.389×10^{-5}	4.028	183.2	0.2203
	10.0	7.520×10^{-5}	1.29	18.48	0.6996
	100.0	8.819×10^{-5}	0.459	1.993	2.307
	1000.0	2.181×10^{-4}	0.2674	0.2735	9.792
		$L=5$, $\alpha_0=90°$			
	E (keV)	gyroperiod (s)	bounce period (s)	drift period (hour)	gyroradius (km)
Protons	1.0	0.2645	215.4	146.4	18.42
	10.0	0.2645	68.12	14.64	58.27
	100.0	0.2645	21.54	1.464	184.3
	1000.0	0.2648	6.818	0.1465	582.8
Electrons	1.0	1.443×10^{-4}	5.035	146.6	0.4302
	10.0	1.469×10^{-4}	1.613	14.78	1.366
	100.0	1.722×10^{-4}	0.5737	1.595	4.505
	1000.0	4.259×10^{-4}	0.3342	0.2188	19.13
		$L=6$, $\alpha_0=90°$			
	E (keV)	gyroperiod (s)	bounce period (s)	drift period (hour)	gyroradius (km)
Protons	1.0	0.457	258.5	122.0	31.84
	10.0	0.4571	81.75	12.2	100.7
	100.0	0.4571	25.85	1.22	318.4
	1000.0	0.4575	8.181	0.1221	1007.0
Electrons	1.0	2.494×10^{-4}	6.042	122.1	0.7434
	10.0	2.538×10^{-4}	1.936	12.32	2.361
	100.0	2.976×10^{-4}	0.6885	1.329	7.785
	1000.0	7.360×10^{-4}	0.4011	0.1823	33.05

Table A 1. (continued).

	E (keV)	gyroperiod (s)	bounce period (s)	drift period (hour)	gyroradius (km)
		$L=7$, $\alpha_0=90°$			
Protons	1.0	0.7258	301.6	104.6	50.56
	10.0	0.7258	95.37	10.46	159.9
	100.0	0.7258	30.16	1.046	505.6
	1000.0	0.7265	9.545	0.1046	1599.0
Electrons	1.0	3.959×10^{-4}	7.049	104.7	1.18
	10.0	4.030×10^{-4}	2.258	10.56	3.749
	100.0	4.726×10^{-4}	0.8032	1.139	12.36
	1000.0	1.168×10^{-3}	0.4679	0.1563	52.48
		$L=8$, $\alpha_0=90°$			
	E (keV)	gyroperiod (s)	bounce period (s)	drift period (hour)	gyroradius (km)
Protons	1.0	1.083	344.7	91.5	75.47
	10.0	1.083	109.0	9.151	238.7
	100.0	1.083	34.47	0.9151	754.7
	1000.0	1.085	10.91	9.155×10^{-2}	2387.0
Electrons	1.0	5.911×10^{-4}	8.056	91.59	1.762
	10.0	6.016×10^{-4}	2.581	9.239	5.597
	100.0	7.055×10^{-4}	0.9179	0.9966	18.45
	1000.0	1.745×10^{-3}	0.5347	0.1368	78.34